Vrije Universiteit Brussel

Faculty of Science and Bio-engineering Sciences
Department of Physics

# N-Body Simulations using HPC

*Re-creating M31's plane of dwarfs from dark matter sub-subhaloes*

Dissertation for the Degree of Bachelor in Physics

Paul Coppin

Promotor: Dr. Garry Angus


MAY 2015

*"The first principle is that you must not fool yourself and you are the easiest person to fool. So you have to be very careful about that. After you've not fooled yourself, it's easy not to fool other scientists. You just have to be honest in a conventional way after that."*

— Richard P. Feynman (Feynman, 2014, p. 343)

"*Physics is really nothing more than a search for ultimate simplicity, but so far all we have is a kind of elegant messiness.*"

— Bill Bryson (Bryson, 2003, p. 110)

ABSTRACT

Observations have shown that a significant number of dwarf galaxies surrounding the Andromeda galaxy are confined to a co-rotating, thin planar structure. In this thesis, a modification of the galaxy group theory is tested, in which the planar structure emerges during a tight fly-by orbit of the satellite galaxy M32 around its host galaxy Andromeda. Dwarf galaxies in the plane are assumed to correspond to the subhaloes of M32, which in turn makes them sub-subhaloes of Andromeda. M32 on the other hand is modelled as one of the largest subhaloes of Andromeda. To test this theory, HPC (High Performance Computing) N-body simulations with over $10^6$ particles are used to simulate the evolution of the system. The thinness of the observed distribution of dwarf galaxies is then trialled against the distribution of sub-subhaloes that results from simulations, by use of a Kolmogorov-Smirnov test. This test was unable to reject the hypothesised origin of the observed dwarf galaxies at any meaningful confidence level.

# ACKNOWLEDGEMENTS

While I was working on this thesis throughout the year, I've received the support and encouragement of numerous people. The first person to whom I'd like to express gratitude, is my promoter Dr. Garry Angus. Without his continuous support, I could have never done the work presented in this thesis. Apart from guiding me in my quest towards understanding and using N-body simulations, I could always come to him to discuss aspects of the project I was working on. It is for this unfaltering readiness to help me, that I am most grateful.

The second person I'd like to thank is my fellow student Jonas Verhellen, with whom I shared a workspace. Whilst confabulating what I was working on proved to be a difficult task for most, Jonas showed interest in and followed my progress during the year. He provided a fresh perspective when I got stuck and offered help whenever I asked for it.

Finally, I would also like to thank Professor Ben Craps and Professor Jan Danckaert for allowing me to use the astrolab as my workspace and providing me access to the Hydra computer cluster. I am also grateful towards my family for supporting me and showing interest in this topic.

CONTENTS

# ACRONYMS

**CDM** Cold Dark Matter

**CIC** Cloud-In-Cell

**CMB** Cosmic Microwave Background

**dSph** Dwarf Spheroidal

**HPC** High Performance Computing

**KS** Kolmogorov–Smirnov

**LMC** Large Magellanic Cloud

**LOFAR** Low-Frequency Array

**MISE** Mean Integrated Square Error

**MW** Milky Way

**NFW** Navarro, Frenk and White

**NGP** Nearest Grid Point

**PAndAS** Pan-Andromeda Archaeological Survey

**PEC** Predict-Evaluate-Correct

**PM** Particle-Mesh

**$P^3M$** Particle-Particle/Particle-Mesh

**PP** Particle-Particle

**SMC** Small Magellanic Cloud

**SPH** Smoothed Particle Hydrodynamics

**TPM** Tree-code Particle-Mesh

**TSC** Triangular Shaped Clouds

**UDF** Uniform Distribution Function

# Part I

# N-BODY CODES

The aim of this section is to explain the various numerical schemes used to approach the N-body problem. A general introduction is given that discusses both the direct and more approximate schemes for numerically solving the orbit of a particle. Furthermore, additional features of N-body codes, such as variable time steps, and methods that allow verification of the result are discussed. Specifically schemes used to model galactic interactions are examined, given that simulating the plane of dwarf galaxies around M31 is the objective of the next section.

# 1 DIRECT GRAVITATIONAL N-BODY SIMULATIONS

## 1.1 INTRODUCTION

In this thesis, the validity of a new spin on an old theory is tested, which aims at providing an origin for the thin plane of dwarfs surrounding the Andromeda galaxy. Verifying the theory requires one to be able to predict the end state of a collision between non-spherical galaxies, that comprise multiple components. Unfortunately, the dynamical evolution of astrophysical systems cannot be traced analytically, except for highly symmetric distributions. A more flexible tool that can simulate the evolution of interacting galaxies is therefore required.

During the last 50 years, N-body simulations have been the backbone of much of the theoretical progress in astrophysics. N-body codes statistically reflect the mass distribution of the components under consideration, by representing them as a system of $N$ particles. The evolution of the system can then be traced by updating the phase space coordinates of the particles using a discrete time step $\Delta t$, meaning that an approximation is used to leap the coordinates of the particles from $t$ to $t + \Delta t$. What follows in chapter one to three is a gentle introduction explaining the workings and features of N-body codes, that will be used to simulate galactic interactions.

## 1.2 DIRECT N-BODY ALGORITHMS

Of all the problems faced in physics these days, calculating the path of a massive particle due to the gravitational interaction with other particles might seem like an easy one. After all, when working in a non-relativistic context, all one has to do is to integrate the set of equations obtained from Newton's second law (1a) combined with Newton's gravitational law (1b)

$$\vec{F} = m \cdot \vec{a} = m \cdot \ddot{\vec{r}} \quad (Sevrin,\ 2012, p.\ 132), \tag{1a}$$

$$\vec{F}_g = G \frac{mM}{r_{12}^3} \vec{r}_{12} \quad (Sevrin,\ 2012, p.\ 103), \tag{1b}$$

where $G$ is Newton's gravitational constant, $M$ and $m$ are the masses of the two respective bodies and $\vec{r}_{12}$ is the vector from particle 1 to particle 2. Unfortunately, obtaining an analytic solution to this problem for general initial conditions is only possible when $N \leq 2$. Though analytic solutions exist for higher values of $N$, these will only occur for certain symmetrical distributions. One example is that of $N$ particles of equal mass rotating in a plane. If these particles are distributed symmetrically on a circle and have velocities such that the centripetal force equals the net gravitational force due to the other particles, the system is in equilibrium and will remain so until disturbed (Carles, 2001, p. 2).

These analytically solvable systems, called choreographies, are however of little use when simulating astrophysical entities such as the Milky Way. Therefore, a more general method is needed to solve the set of $N(N-1)$ equations that are obtained by writing an explicit expression for the acceleration of each

of the $N$ particles, due to their gravitational interaction (1b) with the other $N-1$ particles

$$\vec{a}_i = -\sum_{j=1, j\neq i}^{N} \frac{GM_j}{r_{ij}^3}\vec{r}_{ij} \,. \tag{2}$$

Since $N(N-1) \approx N^2$ for large values of $N$, the computational cost of direct N-body algorithms increases as $\mathcal{O}(N^2)$. Throughout this document, the system of particles will be analysed in a classical way, neglecting relativistic effects. Using this approximation can be justified, since the relativistic deviation will generally be smaller than the error caused by the algorithms used to update the phase space coordinates (Adamek et al., 2013, p. 1).

### 1.2.1 *Euler algorithm*

When using a variable time step $\Delta t$, there are various ways to numerically integrate the equations of motion. The Forward-Euler algorithm calculates the force on a particle at a certain time $t$, and assumes this force is constant during the time-interval $[t, t+\Delta t]$ (Dehnen and Read, 2011, p. 4). A similar though more complicated algorithm called Backward-Euler can be used as well, which uses the assumption that the force at time $t$ is constant during the time-interval $[t-\Delta t, t]$. The Forward-Euler method is in fact the first order Taylor expansion in $t$. Therefore, if $\vec{r}(t)$ and $\dot{\vec{r}}(t)$ are known, the new phase space coordinates become

$$\vec{r}(t+\Delta t) = \vec{r}(t) + \Delta t \cdot \dot{\vec{r}}(t) \,, \tag{3a}$$

$$\dot{\vec{r}}(t+\Delta t) = \dot{\vec{r}}(t) + \Delta t \cdot \ddot{\vec{r}}(t) \,. \tag{3b}$$

This algorithm is accordingly called a first order algorithm, implying that the error per time step is proportional to $(\Delta t)^2$. Though it's not a general rule, higher order algorithms will typically provide better accuracy at a higher computational cost. Since the Euler algorithm has proved to be too inaccurate for most applications, higher order algorithms are often required.

### 1.2.2 *Leapfrog algorithm*

One way to improve upon the Euler algorithm, is to combine Forward- and Backward-Euler into a Leapfrog algorithm. The force on a particle is still assumed to be constant during a time interval $[t-\frac{\Delta t}{2}, t+\frac{\Delta t}{2}]$, but its value is evaluated at time $t$, midway of the interval. Denoting a quantity $a(t = t_0 + i\cdot\Delta t)$ as $a_i$, the new phase space coordinates thus become

$$\vec{r}_{i+1} = \vec{r}_i + \Delta t \cdot \dot{\vec{r}}_{i+1/2} \quad (Young,\ 2014, p.\ 2), \tag{4a}$$

$$\dot{\vec{r}}_{i+1/2} = \dot{\vec{r}}_{i-1/2} + \Delta t \cdot \ddot{\vec{r}}_i \quad (Young,\ 2014, p.\ 2). \tag{4b}$$

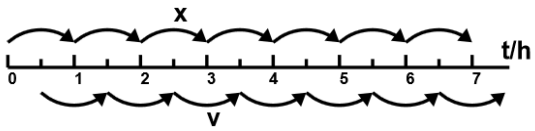


Figure 1: Visualisation of the structure of the Leapfrog algorithm (Quinn et al., 1997).

When starting with initial values $\vec{r}_0$ and $\dot{\vec{r}}_{1/2}$ (which can be obtained by use of equation (45), see Section A.1), the coordinates can be advanced by updating

the position and calculating the updated force at integer times. Advancing $t$ by $\frac{\Delta t}{2}$ and updating the velocity then closes the scheme. Another second order algorithm can be obtained be rewriting (4a) and (4b) as

$$\vec{r}_{i+1} = \vec{r}_i + \Delta t \cdot \dot{\vec{r}}_i + \frac{(\Delta t)^2}{2} \ddot{\vec{r}}_i \ , \tag{5a}$$

$$\dot{\vec{r}}_{i+1/2} = \dot{\vec{r}}_i + \frac{\Delta t}{2} \ddot{\vec{r}}_i \ . \tag{5b}$$

Velocities are now updates twice over $\frac{\Delta t}{2}$ each time the position is updated over $\Delta t$. This derivation and the time-reversibility of the Leapfrog algorithm is derived in Section A.1. Equations (5a) and (5b) can be seen as a second order Taylor expansion of $\vec{r}$. Accordingly, it is a second order algorithm and errors are proportional to $(\Delta t)^3$.

Though it is possible to keep on constructing higher order algorithms (that make extra corrections to the equations of motion), the supplementary computational cost generally outweighs the improved accuracy. One way to increase accuracy at a low computational cost, is by constructing a fourth order Hermite algorithm (see Section A.2). A nice feature of this solution is that higher order derivatives of $\vec{r}$ can be written as a function of lower order derivatives of $\vec{r}$. This means that the computational cost of the algorithm will remain $\mathcal{O}(N^2)$, as was shown by Nitadori and Makino (2008), who were able to devise an eighth order scheme where the number of force calculations increased by about a factor two compared to a fourth order scheme.

# 2 APPROXIMATION SCHEMES

An obvious way to calculate the orbit of a particle, would be to use the Particle-Particle (PP) method. This can be done by using one of the algorithms from Chapter 1 and applying it to each particle individually. During a time step, the movement of each particle is then calculated by computing its pairwise interaction with the other $N-1$ particles. This brute force method is however not a viable option for simulations with $N > 1000$ particles, because the computational cost increases as $\mathcal{O}(N^2)$ (Sellwood, 1987, p. 162).

Computing the gravitational force at each particles position is generally the most time consuming component of N-body codes and therefore central to all schemes updating the phase space coordinates. It is thus worthwhile to produce an efficient algorithm that is accurate for large $N$. A fundamental limitation to the accuracy of these algorithms is set by the number of particles that can be efficiently used. This means the number of particles for which a simulation will finish within a reasonable amount of time.

## 2.1 TREE ALGORITHMS

Consider a particle $p$ that is prone to forces from a group of particles that are inside a sphere of radius $r$. If the distance between $p$ and the centre of the sphere is much larger than $r$, the force on $p$ can be approximated by that of the centre of mass of the particles inside the sphere. This approximation would moreover be exact if the particles were distributed spherically symmetrical, as shown by Newton's first theorem (Binney and Tremaine, 2011, p. 60). Though perfect spherical symmetry does not occur in simulations, using this technique allows one to maintain a roughly constant force error, while computing forces that are both close and long range (Springel, 2005, p. 7).

### 2.1.1 *Cell-opening criterion*

To determine whether a group of particles located in a cubic cell of size $l$ is at ample distance to be approximated by their centre of mass, tree algorithms make use of cell-opening criteria. A simple but powerful criterion was devised by Barnes

$$d > \frac{l}{\theta} + \delta \quad (Dubinski,\ 1996, p.\ 4), \tag{6}$$

where $d$ is the distance from the particle to the centre of a distant cell and $\delta$ is the distance between the centre of the cell and the centre of mass of the elements in it. Choosing a value for $\theta$ then determines the accuracy of the approximation. The smaller $\theta$, the less likely that the cell is at a large enough distance and thus the better the approximation. The factor $\delta$ prevents aberrations when the centre of mass lies near the edge of the cell (Dubinski, 1996, p. 4).

Another example of cell-opening criteria are those used in the N-body code GADGET-2. For a cubic cell of size $l$ containing mass $M$ at distance $r$, the criteria consists of the two inequalities

$$\frac{GM}{r^2}\left(\frac{l}{r}\right)^2 \leq \alpha \cdot |\vec{a}| \quad (Springel, 2005, p.\ 6), \tag{7a}$$

$$|\vec{r}_k - \vec{c}_k| \leq 0.6 \cdot l \quad (Springel, 2005, p.\ 7). \tag{7b}$$

Here, $\alpha$ determines the accuracy and $\vec{a}$ is the total acceleration of the particle during the last time step. The first criterion therefore requires cells that exert a large fraction of the total force on the particle, to be at an ample distance. In equation (7b), $\vec{c}$ is the centre of the cell, $\vec{r}$ the position of the particle and $k \in \{x, y, z\}$. The second criterion thus requires the particle to lie outside the cell, preventing large errors if a particle were to fall inside the cell (Springel, 2005, p. 7).

### 2.1.2 *Barnes-Hut method*

To group particles together, the Barnes-Hut algorithm uses an octree. An octree can be built by creating a cube that surrounds all the particles. If more than one particle lies inside the cube, it splits into eight new equal sized cubes that lie inside the first cube. Each new cube thus has a side half of the side of the first cube. This procedure can be applied recursively until each particle lies inside a separate box. The largest cube is then called the root, while the cubes containing one particle are called leaves (Barnes and Hut, 1986, p.447).

The second step in the Barnes-Hut method is to calculate the centre of mass and total mass of all the non-empty cubes at each level of the tree. This is done from leaves to root to reduce computations. Finally, the force on each particle can then be determined by traversing the tree starting from the root. Each cube is broken down into subgroups unless the cube is a leaf or satisfies the cell-opening criterion. In that case, the centre of mass of the cube is used to determine the force (Barnes and Hut, 1986, p. 447).

During the next time step, these three steps have to be repeated and the tree has to be rebuilt from scratch. Nevertheless, the algorithm increases only as $\mathcal{O}(Nlog(N))$ and is therefore a huge improvement over the PP method (Sellwood, 1987, p. 163). One of the drawbacks from this method is that the cubes are positioned symmetrically and are therefore often not centred around large concentrations of particles. In addition, the forces two particles exert on one another do not have to be equal and opposite, implying that momentum is not strictly conserved (Sellwood, 1987, p. 179). An example of more complicated tree algorithm that tackles these issues is discussed in Section B.1.

## 2.2 PARTICLE MESH ALGORITHMS

### 2.2.1 *Poisson's equation for gravity*

Although tree algorithms are a very effective way of reducing computations, they are often not economical enough since their run time increases as $\mathcal{O}(Nlog(N))$. Computations can be sped up by introducing a grid. A Cartesian grid for example, is a collection of adjacent points that are separated by a constant distance $d$, constructing cubes/cells of side $d$. Though other distributions such as spherical polar grids can be used, the density of grid points is then no longer constant.

While symmetric distributions such as single galaxies might benefit from this (by choosing a grid that reflects the same symmetry as the galaxy), the non constant density of grid points will introduce a bias in simulations where such symmetry is not present. From now on, the grid will be assumed to be Cartesian, since the aim of this dissertation is to study galactic interactions (Sellwood, 1987, p. 176).

To deal with regions that have a relatively high density of particles, an adaptive mesh can be employed. Grid cells that lie in dense regions will then split into eight new cubic cells, that lie inside the original cell. This method can be applied recursively until each grid cell contains no more than a given number of particles (Springel, 2005, p. 1106).

When using grid algorithms, forces are no longer calculated at each point where a particle resides, but only at grid points. This Particle-Mesh (PM) method is therefore only meaningful when using considerably fewer grid points than there are particles. Downsides of using a grid are that the spatial resolution of a simulation is limited to approximately the distance between grid points and that the force on particles that go outside the grid can no longer be computed (Sellwood, 1987, p. 165). This last issue can be resolved in cosmological simulations, which often employ periodic boundary conditions. If a particle's coordinate $\vec{r}_i$ exceeds the edge of the grid, it is set equal to $-\vec{r}_i$. The particle will thus leave the grid on one side and re-enter it on the other. Using this approximation can be justified if the length of the grid corresponds to a distance of the order of 100 $Mpc$, because the Universe is homogeneous and isotropic at this scale (Craps and Waelkens, 2013, p. 8).

The potential $\Phi$ at each grid point $\vec{r}$ can be determined by rewriting equation (1b) for a continuous mass distribution. The force $\vec{g}$ acting on a particle of unit mass is then

$$\vec{g}(\vec{r}) = -G \int \rho(\vec{s}) \frac{\vec{r}-\vec{s}}{|\vec{r}-\vec{s}|^3} d^3\vec{s}\,, \tag{8}$$

where the integral is carried out over all space and $\rho$ denotes the mass density. Using the identity (9a), equation (8) can be rewritten as Gauss's law for gravity (9b)

$$\vec{\nabla} \cdot \left( \frac{\vec{r}}{r^3} \right) = 4\pi\delta(\vec{r}) \quad (Griffiths,\ 1998, p.\ 50), \tag{9a}$$

$$\vec{\nabla} \cdot \vec{g}(\vec{r}) = -4\pi G\rho(\vec{r}) \quad (Rodriguezet\ al.,\ 2014, p.\ 3). \tag{9b}$$

Since gravity is a central, and therefore conservative, force it is possible to find a potential $\Phi$ related to $\vec{g}$ by equation (10a). Equation (9b) can thus be rewritten as Poisson's equation for gravity (10b)

$$\vec{g} = -\vec{\nabla}\Phi \quad (Sevrin,\ 2012, p.\ 125), \tag{10a}$$

$$\nabla^2\Phi = 4\pi G\rho \quad (Rodriguezet\ al.,\ 2014, p.\ 3). \tag{10b}$$

### 2.2.2 *Allocating mass to grid cells*

When using a grid, an approximation of the mass density can be obtained by allocating the mass of each particle to one or more grid cells. The mass density in grid cell $p$ then becomes

$$\rho_p = \frac{1}{d^3} \sum_{i=1}^{n} m_i \cdot W_p(\vec{r}_i)\,, \tag{11}$$

where the summation is over all particles $\vec{r}_i$ with corresponding masses $m_i$, $d$ is the side of the grid cells and $W_p(\vec{r}_i)$ is the percentage of mass of particle $i$ allocated to grid cell $p$.

The easiest way of distributing the mass of particles over all grid cells is by using the Nearest Grid Point (NGP) technique. The mass of grid cell $p$ then becomes the total mass of all particles that lie inside that grid cell. This method can be seen as an interpolation of zeroth order.

An interpolation of first order is the Cloud-In-Cell (CIC) method. This technique distributes the mass of a particle over the eight nearest grid cells. The amount of mass allocated to a grid cell is determined by calculating the overlapping volume $V$ between a cube of side $d$ centred around the particle and the grid cell. If the particle has mass $m$, the grid cell is allocated a fraction $\frac{V}{d^3}$ of that mass (Springel, 2014, p. 22). These methods of allocating mass to grid points can be extended to higher orders (see Section B.2).

### 2.2.3 *Determining the potential in grid points*

To obtain the potential on grid points, equation (10b) has to be solved using the discrete density function $\rho$ obtained in Section 2.2.2. An evident way to solve (10b) in the one dimensional case, would be to approximate the derivative by

$$\left(\frac{\partial^2\Phi}{\partial x^2}\right)_i \approx \frac{\Phi_{i+1} - 2\Phi_i + \Phi_{i-1}}{d^2}, \tag{12}$$

where $d$ equals the grid spacing and $i$ runs over all $N$ grid points. Equation (12) can however not be applied to points that lie on the edge of the grid, since either $\Phi_{i+1}$ or $\Phi_{i-1}$ will not exist. For galactic simulations in which all the mass lies near the centre of the grid, the potential at those points can then be approximated as $\frac{GM}{r}$. Substituting equation (12) into (10b) results in a system of $N$ linear equations with $N$ unknowns ($\Phi_i$). This system can be solved in $\mathcal{O}(N^3)$ and is therefore too computationally expensive for simulations with large amounts of particles (Springel, 2014, p. 36).

Fortunately, it is possible to compute $\Phi$ in $\mathcal{O}(Nlog(N))$ time by using the Fourier transform. Consider the case of a continuous density function $\rho$ in a box of size $d$ that has periodic boundary conditions. Writing both $\rho$ an $\Phi$ as a Fourier series and substituting this into equations (10b) yields

$$\nabla^2\left(\sum_{\vec{k}} \Phi_{\vec{k}} e^{i\vec{k}\cdot\vec{x}}\right) = 4\pi G\left(\sum_{\vec{k}} \rho_{\vec{k}} e^{i\vec{k}\cdot\vec{x}}\right), \tag{13}$$

where $\vec{k} \in \frac{2\pi}{d}(n_1, n_2, n_3)$ and $n_i \in \mathbb{Z}$. Carrying out the Laplacian and using the orthogonality of the different modes then gives the coefficients $\Phi_k$ and thus the total density $\Phi$ by

$$\Phi_{\vec{k}} = -\frac{4\pi G}{\vec{k}^2}\rho_{\vec{k}} \quad (Springel, 2014, p. 30). \tag{14}$$

These techniques can be extended to the case of a three dimensional grid with $N^3$ grid points. The coefficients of the Fourier transform of $\rho$ are then obtained

be replacing equation (15a) by (15b), where the integral over a box $V$ of size $L^3$ is converted into a discrete sum over all grid points $\vec{p}$

$$\rho_{\vec{k}} = \frac{1}{L^3}\int_V \rho(\vec{x})e^{-i\vec{k}\cdot\vec{x}}d^3\vec{x} \quad (Springel, 2014, p.\ 29), \tag{15a}$$

$$\rho_{\vec{k}} = \frac{1}{N^3}\sum_{\vec{p}} \rho_{\vec{p}}e^{-i\vec{k}\cdot\vec{x}_{\vec{p}}} \quad (Springel, 2014, p.\ 30). \tag{15b}$$

Due to this discretisation, the possible values of $n_i$ that determine $\vec{k}$ are now restricted to $\left(-\frac{N}{2},...,-1,0,1,...,\frac{N}{2}-1\right)$. Furthermore, the requirement that $\Phi$ has to be real implies that $\rho_{\vec{k}} = \rho^*_{-\vec{k}}$. This correlation between between the coefficients of the Fourier series reduces the number of computations necessary by a factor two. For a one dimensional grid with $N = 2^m$ grid points, this same 'trick' can be applied $m$ times and thus accounts for the speed of grid algorithms (Bodenheimer et al., 2006, p. 101).

### 2.2.4 *Interpolating accelerations*

Once the gravitational potential has been determined on the grid points. The next step is to determine the acceleration $\vec{a}_{i,j,k}$ a particle of unit mass lying on grid point $(i,j,k)$ would experience. This information can then be used to interpolate the acceleration on a particle that lies in between grid points.

For each grid point, $\vec{a}_{i,j,k}$ can be determined by explicitly calculating the right side of equation (10a). Since $\Phi$ is now a discrete function, the acceleration at $(i,j,k)$ in the $x$ direction can be approximated by finite differencing

$$\vec{a}^x_{i,j,k} = -\frac{\Phi_{i+1,j,k} - \Phi_{i-1,j,k}}{2d}, \tag{16}$$

where $d$ is the grid spacing and the error is of order $\mathcal{O}(d^2)$ (Fornberg, 1988, p. 702). Depending on the order of approximation used to allocate mass to grid points and the overall accuracy of the algorithm, it might be feasible to use approximations of higher order. These higher order algorithms are discussed in Section B.3. Naturally, the acceleration in the $y$ and $z$ direction can be calculated analogously by varying respectively the second and third index of $\Phi_{i,j,k}$.

The force on each individual particle can now be interpolated by the accelerations of the surrounding grid points. A particle with mass $m$ located at $\vec{x}$ then experiences a total force

$$\vec{F}(\vec{x}) = m\sum_{p} \vec{a}_{\vec{p}} W_p(\vec{r}_i), \tag{17}$$

where the summation runs over all grid points $p$ and $W_p$ is the same function as in equation (11). Though it is possible to replace $W_p$ by a different function, this is not advisable. Using the same function to allocate mass to grid points as to interpolate the forces on individual masses from those grid points results in vanishing self-forces. This means that a particle cannot accelerate by interacting with itself. Furthermore, the forces two particles exert on each other are equal in magnitude and opposite in direction (Springel, 2014, p. 26). A proof of these two claims is provided in Section B.4.

## 2.3 ADDITIONAL SCHEMES

N-Body codes used to simulate galaxies are often neither purely based on the PP, tree nor grid technique, but a combination of those schemes. Two specific

examples are the Particle-Particle/Particle-Mesh ($P^3M$) and Tree-code Particle-Mesh (TPM) method.

The $P^3M$ uses the PM method to calculate the long-range force, which is defined as the force due to particles at a distance larger than $r_e$. This value $r_e$ is typically chosen to be two or three times the size of a grid cell (Yoshikawa and Fukushige, 2005, p. 4). The short range force due to particles closer than $r_e$ is then respectively calculated by use of the PP method. For systems in which situations occur where particles are highly clustered together, the $P^3M$ method is not a viable option. The calculation of the short range force then becomes too computationally expensive, leaving the TPM method as the preferred alternative (Bagla, 2002, p. 2).

When using the $P^3M$ method, the first step is to apply the PM method. For an arbitrary particle $p$, this results in a force $\vec{F}_{PM}$. The total force $\vec{F}_{tot}$ on that particle then becomes

$$\vec{F}_{tot} = \vec{F}_{PM} + \sum_{i=1}^{k} \vec{F}_{i,sr} - \vec{F}_{i,PM,sr} \ , \tag{18}$$

where the summation runs over all particles closer than $r_e$ and $\vec{F}_{i,sr}$ is the force obtained by the PP method for those particles. The contribution of those particles to $\vec{F}_{PM}$ is then subtracted by $\vec{F}_{i,PM,sr}$. Since the PM method treats particles as a mass cloud, the functional form of $\vec{F}_{i,PM,sr}$ will depend on the choice of $W_p$ (defined in Section 2.2.2) used when applying the PM method (Yoshikawa and Fukushige, 2005, p. 5). A computationally less expensive technique is to calculate $\vec{F}_{i,sr}$ by use of a tree algorithm instead of the PP method.

The TPM method is similar to the $P^3M$ method, but only separates forces in regions where the particle density is higher than a given threshold. Inside those regions, long-range forces are computed by the PM method and short-range forces by a tree algorithm. Outside those regions, all forces are computed using the PM method (Yoshikawa and Fukushige, 2005, p. 7).

# 3 FEATURES OF GRAVITATIONAL ALGORITHMS

## 3.1 TIME STEPPING LEAPFROG

When using the PP or tree method, a logical choice would be to use a constant time step to advance the coordinates of all particles. Though this is by far the least complicated option, advanced N-body codes typically use time steps that can vary from particle to particle. Consider for example the simulation of a galactic disk. While a sufficiently small time step is needed to simulate interactions between close by particles at the centre, the force between a particle at the centre and the edge will vary significantly slower. Computations can thus be sped up by using different time steps, depending on the rate at which the force between two particles changes (Sellwood, 1987, p. 180).

One way of realizing such a system is by dividing the simulation into multiple zones depending on the density of particles. Consider for example the Leapfrog algorithm in the PP-method. Particles in the zone corresponding to the lowest density are then advanced by a time step $\Delta t$, while particles in other zones are advanced multiple times with time step $\frac{\Delta t}{n}$, where $n \in \mathbb{N}$ increases with density. In dense regions where the time step is smaller than $\Delta t$, the computation of the force on a particle requires the position of the particles in less dense regions at times between $t$ and $\Delta t$. These positions can be approximated by interpolating the particles position between $t$ and $\Delta t$ (Sellwood, 1987, p. 180).

Apart from the ease with which a variable time step can be introduced, the Leapfrog algorithm also requires considerably fewer force computations than higher order algorithms. Its most important feature is however that it's a symplectic integrator, meaning it offers the exact solution to a discrete Hamiltonian. This implies that for a time-independent Hamiltonian, the Leapfrog integrator will conserve the total energy. In axisymmetric systems it also preserves angular momentum. Consider for example figure 2, in which the position of a particle was advanced over 16 Kepler orbits ($e = 0.5$) using a Leapfrog algorithm (squares) and fourth order Runge-Kutta algorithm (crosses) with the same constant time step. Figure 2 shows the radial velocity of the particle $v_r$ versus radius $r$. Even though the Runge-Kutta algorithm required four times more force calculations, the Leapfrog algorithm clearly better approximates the exact solution (solid line) (Quinn et al., 1997, p. 2).

Fortunately, it is possible to construct multiple time step symplectic integrators that preserve important quantities such as total energy and are time reversible (Duncan et al., 1998, p. 2077). An example of such an integrator is used in GADGET-2, where time steps are chosen to be $\frac{\Delta t_{max}}{2^n}$ with $n \in \mathbb{N}$ and $\Delta t_{max}$ a constant determining the maximum time step. The time step used for particle $p$ is less than or equal to

$$\Delta t_{grav} = min\left(\Delta t_{max}, \sqrt{\frac{2\eta\epsilon}{|\vec{a}_p|}}\right), \tag{19}$$

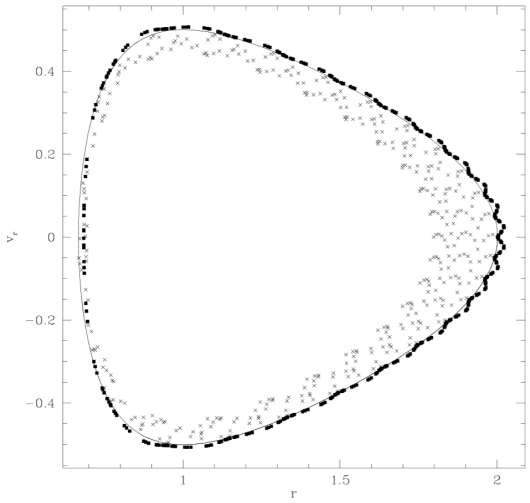


Figure 2: Evolution of the radial distance $r$ and radial velocity $v_r$ of a particle over 16 Kepler orbits ($e = 0.5$). Due to its symplectic nature, the second order Leapfrog algorithm (squares) better approximates the exact solution (solid line) than a fourth order Runge-Kutta algorithm (crosses) (Quinn et al., 1997, p. 3).

where $\eta$ is a constant determining the accuracy, $\epsilon$ the gravitational softening and $\vec{a}_p$ the particle's acceleration. To prevent infinitely small steps, a value $\Delta t_{min}$ can be set below which $\Delta t_{grav}$ cannot decrease. Furthermore, a particle is allowed to increase its time step only if it synchronizes with the time step hierarchy. When combining a tree and grid scheme, the code uses the above procedure for time stepping the tree and the constant time step $\Delta t_{max}$ for the grid (Springel, 2005, p. 1116).

## 3.2 GRAVITATIONAL SOFTENING

A drawback of simulating large systems, such as the Milky Way, is that the number of particles used in the simulation is much smaller than the actual number of particles in the system. As a results, the simulations effected in Chapter 5 used particles that have a mass that is six orders of magnitude larger than a solar mass. Representing stars, gas or dark matter as such heavy point like particles allows for unrealistic close encounters causing strong deflections (Sellwood, 1987, p. 156). One way to solve this problem is by replacing the Newtonian potential around a particle of mass $M$ by

$$\Phi(r) = -G\frac{M}{\left(r^2+\epsilon^2\right)^{1/2}} \quad (Sellwood,\ 1987, p.\ 156). \tag{20}$$

This softened potential correspond to a softened force with corresponding acceleration

$$\vec{a} = -G\frac{M}{\left(r^2+\epsilon^2\right)^{3/2}}\vec{r}\,. \tag{21}$$

Depending on the distribution, the optimal value of $\epsilon$ is typically 1.5 to 2 times smaller than the average distance between particles in the most dens region (see Appendix C for the determination of $\epsilon$). Similar to the CIC method, replacing the real by the softened potential can be regarded as replacing a point mass by a finite mass 'cloud'. The shape of this mass distribution can be calculated by applying Poisson's equation for gravity (10b) to the softened potential

and yields a Plummer sphere mass distribution (Rodionov and Sotnikova, 2005, p. 3), which contains 85% of the mass inside $3\epsilon$

$$\rho(r) = \frac{3M}{4\pi} \frac{\epsilon^2}{\left(r^2 + \epsilon^2\right)^{5/2}} \,. \tag{22}$$

Softened forces are thus used in simulations that make use of the PP or tree method and replace the unrealistic heavy point masses by a continuous mass distribution. When using a grid, the interaction of two particles less than a few grid spacings apart (depending on the form of $W_p$ in Section 2.2.2) is suppressed due to the nature of the grid. Introducing softened potentials is therefore not necessary for grid algorithms (Sellwood, 1987, p. 156).

## 3.3 VERIFYING RESULTS

One tricky question that remains unanswered is how the end result of a simulation holds up against what would have happened in real life. A steady check is to compute quantities that should be conserved, such as total energy and (angular) momentum, and analyze their time dependance. Even when using a symplectic integrator, these tests might fail due to an unfounded choice of variables such as the time step or softening length (Hayes, 1995, p. 2).

A stronger check is to set up a simulation in which starting from the initial conditions, the orbits of the particles can be solved analytically. For such a simulation, the dependency of the result on numerical parameters can be checked by varying the total number of particles, grid size and time step parameters. Time reversibility can be another steady check, especially when it's not a formal property of the integrator. A more demanding but reliable verification is to use different codes to propagate particles starting from the same initial conditions (Sellwood, 1987, p. 183).

Errors induced by the use of discrete time steps, values of $N$ that are typically several orders of magnitude smaller than the number of bodies in the system and computers producing round off errors, ensure the results of simulations will never be exact. These errors will be magnified exponentially and thus ensure the chaotic nature of N-body simulations. Obtaining the exact position or velocity of particles is however not the goal in simulations where $N$ is large. It seems that despite these 'statistical' fluctuations, N-body codes have become reliable enough to model the time evolution of the overall distribution of a system of particles (Hayes, 1995, p. 1).

# Part II

## CO-ROTATING DWARFS AROUND M31

This section aims to provide a plausible explanation for the thin plane of co-rotating dwarfs around the Andromeda galaxy. A general code that produces the initial conditions of disk galaxies, consisting of a halo, bulge and stellar and gaseous disk in equilibrium, is devised. These model galaxies are then used to simulate a fly-by encounter between Andromeda, M32 and M32's subhaloes. The resulting distribution is used to quantify the likelihood that the dispersal of M32's subhaloes is the origin of the co-rotating plane of dwarfs.

# 4 DWARF GALAXY PLANES

## 4.1 OBSERVED STRUCTURE OF DWARF GALAXIES

The Local Group contains two major galaxies with total masses (dark matter and baryons) $M > 10^{12} M_{\odot}$: the Milky Way (MW) and Andromeda (M31). Both galaxies are orbited by a number of dwarf galaxies (McConnachie, 2012), such as: Fornax, Ursa Minor and Draco for the MW ; And I, And III and NGC 147 for M31. They are also host to a few larger satellite galaxies, such as the Magellanic Clouds (MCs) for the MW and M32 and M33 (also known as Triangulum) for M31. The exact number of dwarfs that are part of the Local Group is still uncertain, but keeps increasing with the detection of faint and ultra faint galaxies (Koposov et al., 2015). Many of these low luminosity galaxies orbiting the MW or M31 are dwarf spheroidal (dSph) galaxies. Recent observations have shown that the distribution of dSph galaxies is highly non-isotropic and exhibits a planar structure for both the MW and M31 (Pawlowski et al., 2013, p. 1929). Though farther away, the spatial distribution of satellites around M31 is easier to observe, since only a small region of the sky must be surveyed. It is for this reason that the rest of this chapter and the simulations carried out in Chapter 6 will focus on M31 and the system of dwarfs around it.

The Pan-Andromeda Archaeological Survey (PAndAS; McConnachie et al. (2009)), which covered an area of roughly 400 square degrees (1% of the sky's surface), was carried out to detect stellar objects at a projected distance of up to 150 $kpc$ from M31. Their observations showed that based on an extrapolated flat number-density profile, there are $88 \pm 20$ dSph satellites orbiting M31 inside a 300 $kpc$ radius, from which only about one fourth has currently been discovered. For dSph galaxies that were observed by PAndAS and lie farther than 2.5 degrees from M31, the distance to those galaxies was measured with the tip of the red giant branch method (Lee et al., 1993). These distances typically have an accuracy of 5% ($\pm 39 kpc$) and resulted in the $3D$ position of 27 dSph galaxies around M31.

Based on these observations, it was discovered that 15 out of the 27 dwarfs are confined to an extremely thin, but radially extended disk that is moreover rotationally supported. This feature is displayed in figure 3, where the red circles indicate the galaxies belonging the the planar structure. Furthermore, most of those 15 dwarfs lie on the same side of M31. A Monte Carlo analysis by Ibata et al. (2013) showed that the probability of such an alignment occurring at random is less than 0.13%. Additionally, 13 out of the 15 dwarfs share the same sense of rotation. The root-mean-squared thickness of the planar structure belonging to those 13 dwarfs was found to be less than 14.1 $kpc$ with 99% confidence (Ibata et al., 2013).

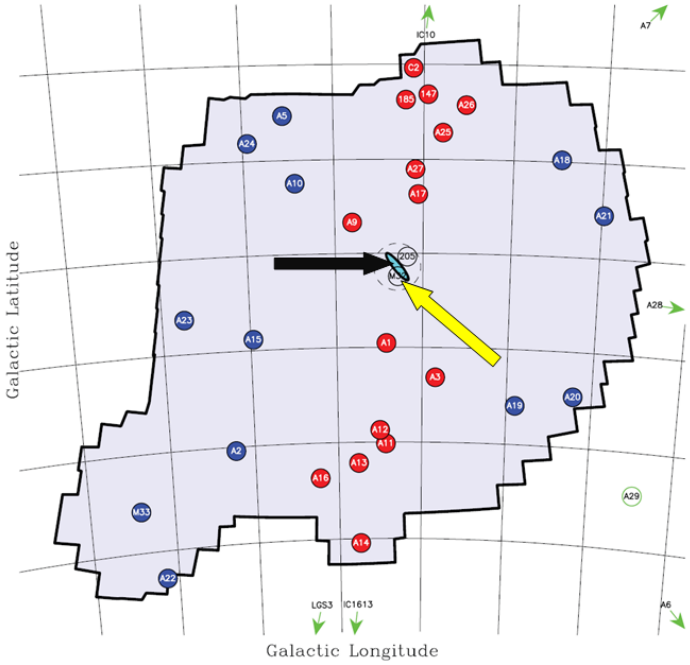


Figure 3: Distribution of dwarfs around M31. Red circles indicate dwarfs belonging to the planar structure (Ibata et al., 2013). M31 and M32 are indicated respectively by a black and yellow arrow.

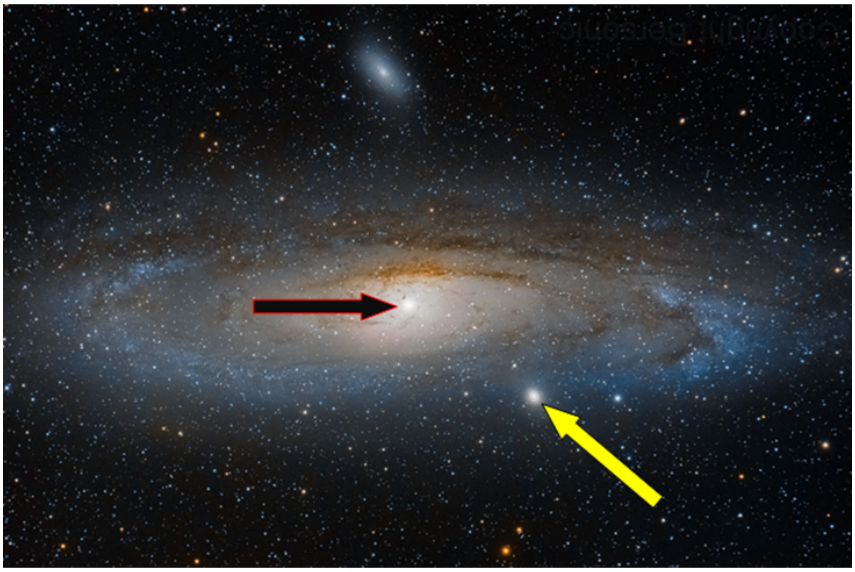

Figure 4: Close-up of M31 as observed in the visual bandpass (Bers, 2014). M31 and M32 are indicated respectively by a black and yellow arrow.

## 4.2 COSMOLOGICAL SIMULATIONS

A theory that has been well able to describe the current state and evolution of our universe, is the ΛCDM model (Spergel et al., 2007). While Λ refers to Einstein's cosmological constant used to explain the accelerated expansion of the universe, CDM is an acronym for cold dark matter. Based on this theory, the structure observed in the universe today formed bottom-up, i.e. first small scale structures formed which later merged into larger structures (Libeskind et al., 2013).

To explain the observed distribution of satellite galaxies, it is necessary to first discuss the structure that emerges from cosmological simulations. Unlike galactic simulations, cosmological simulations are set in an expanding universe. Their initial conditions, which typically are chosen at $z = 50$ (long after the "recombination" of electrons and protons and the last scattering surface of the CMB), can be generated after understanding the initial distribution of plasma, radiation and dark matter after the big bang. While the dark matter could collapse, forming potential wells, the densities of the plasma and radiation were initially oscillating, failing to collapse due to the radiation pressure (Craps and Waelkens, 2013, p. 79). About 400.000 years ($z \sim 1000$) after the big bang, the radiation in the Universe had cooled down enough to allow the "recombination" of nuclei and electrons. The distribution of over- and underdensities of the plasma and radiation at that time have been well-modelled in the analysis of the anisotropies of the cosmic background radiation, which was measured with great accuracy (Planck Collaboration et al., 2014). As long as $|\frac{\rho-\widehat{\rho}}{\widehat{\rho}}| \ll 1$, where $\rho$ is the density of the over/under dense region and $\widehat{\rho}$ the average density, $\rho$ will evolve linearly as a function of time and the evolution of the Universe can be modelled analytically. Once $\rho(t)$ starts evolving non-linearly, cosmological simulations are needed to describe the further evolution of our Universe.

Cosmological simulations (Klypin et al., 1999; Moore et al., 1999) showed the formation of dark matter haloes and revealed their internal substructure, which are thus predictions of the ΛCDM model. This internal structure consists of gravitationally bound substructures, called subhaloes. Subhaloes can in turn have their own substructure. These subhaloes of subhaloes are accordingly called sub-subhaloes of the main halo. The Aquarius Project (Springel et al., 2008), being particle wise the largest of those simulations (using more than $4 \cdot 10^9$ particles), was able to detect up to four generations of subhaloes nested inside the main halo. The distribution of sub-subhaloes around a subhalo in the Aquarius project was found to be well described by the Einasto profile

$$\rho(r) = c_1 \exp\left\{\frac{-2}{\alpha}\left[\left(\frac{r}{c_2}\right)^{\alpha} - 1\right]\right\}, \tag{23}$$

where $\alpha = 0.678$ and $c_1$ and $c_2$ are constants fitted to the host subhalo. A plot, based on the Aquarius project, displaying the number of subhaloes per halo as a function of mass is displayed by the black line in figure 5. The red, blue and green lines meanwhile display this same relation for the number of subsubhaloes per subhalo for three different simulations.

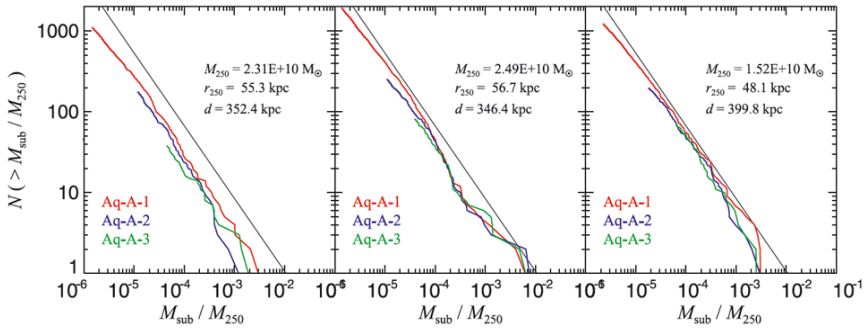


Figure 5: Number of sub-subhaloes N where the ratio of their mass ($M_{sub}$) to their host's ($M_{250}$) is larger than $\frac{M_{sub}}{M_{250}}$. This is shown for sub-subhaloes around a chosen subhalo (blue, red & green lines representing simulations of different resolution, but with the same initial conditions). Only sub-subhaloes inside the virial radius $r_{250}$ of the subhalo are counted. The distance $d$ between the subhalo and host halo is given in each panel. The same relation is shown for subhaloes with respect to the main halo (black line) (Springel et al., 2008).

### 4.3 THE TOO BIG TO FAIL PROBLEM

Subhaloes, having a larger mass density than their surroundings, should in some cases be able to accrete enough gas to allow star formation. They are therefore considered to be main origin of dSph galaxies. Based on ΛCDM simulations, the number of expected satellites is however more than one order of magnitude higher than the number of dwarfs that has currently been observed (Metz et al., 2009, p. 269). An important problem that remains to be solved is therefore to relate the few currently observed dwarf galaxies to the substructure of the halo and explain why so many subhaloes remain dark.

The first out of two options is that the subhaloes exist, but have have not yet been observed. Kinematic studies of ultra-faint galaxies ($L < 10^5 L_\odot$) indicate they are strongly dark matter dominated and could have mass-to-light ratios of up to $10^5 - 10^8$, if they are hosted by the most massive subhaloes (Boylan-Kolchin et al., 2011, p. 43). Even subhaloes in the MW that are completely dark might be detectable due to their tidal influence on the HI disk. The question then remains how observations could have missed the hundreds of satellites or why the subhaloes did not produce any stars (Klypin et al., 1999, p. 90).

The second option is that the ΛCDM simulations are incorrect in their prediction of the number of subhaloes. While it is also possible that the subhaloes of the MW are simply a statistical aberration, this seems unlikely since M31's system exhibits the same behaviour (Boylan-Kolchin et al., 2011, p. 43). Possible solutions that could explain the inhibited formation of subhaloes are assuming that dark matter particles are warm instead of cold or assuming that dark matter particles can self annihilate (D'Onghia and Lake, 2008, p. 61).

#### 4.3.1 *Current theories*

An evident way to associate the observed dSph galaxies to dark matter subhaloes, would be to postulate that only the most massive subhaloes are able to form bright dwarf galaxies. This theory was tested by Walker et al. (2007), by calculating the mass of dwarf galaxies from stellar kinematics using the

methods outlined in Section 5.3.2. These masses turned out to be generally much lower than those of the most massive subhaloes in the Aquarius Project (Boylan-Kolchin et al., 2012, p. 1203). The planar distribution would furthermore be highly unlikely, since a more isotropic distribution would be expected.

A second theory is that dSph galaxies form around dark matter subhaloes, which are then accreted along dark matter filaments (Libeskind et al., 2005, p. 146). N-body simulations however showed that neither the planar structure nor the coherent rotation were reproduced in accordance with observations (Pawlowski et al., 2013, p. 1929).

D'Onghia and Lake (2008) provided a third theory, that assumes that the distribution of dSph galaxies around the MW originates from a compact group of dwarf galaxies falling onto the MW's halo. One positive feature of this theory is that it has the potential to explain both the planar structure and rotation of the dSph galaxies around the MW. Their theory however requires that the subhaloes of the MW's halo stay dark, while groups of dwarfs falling into a host halo light up. Although disputed by Metz et al. (2009), their claim is that almost all subhaloes stay dark, because gas gets blown out of the subhaloes before they can light up. A counterargument against this theory is that no compact groups of dwarf galaxies have been observed in or around the Local Group, making them quite rare. Assuming that the dwarfs around M31 originate from the same phenomenon then requires two compact groups simultaneously falling onto the MW and M31 (Metz et al., 2009, p. 273).

### 4.3.2 *(Sub)-subhaloes as origin*

A subtle modification of the galaxy group theory was proposed by Dr. Garry Angus. Consider one of the most massive subhaloes of M31 ($M_{sub} \approx 0.01 M_{halo}$, see figure 5) located at the edge of the halo ($d \approx 450\ kpc$). The Aquarius Project showed that this subhalo should have multiple sub-subhaloes. While the masses of the largest subhaloes are in accordance with the mass of M32 and the SMC, the masses of the sub-subhaloes ($M < 10^{-5} M_{halo}$) are likewise comparable to that of the other dSph galaxies. The theory therefore states that the planar structure around M31 and the MW originated from sub-subhaloes nested inside one subhalo (corresponding to M32 or the SMC), which are the counterparts of the observed dwarf galaxies.

From redshift 20 to 10, the first stars in the MW formed. Due to the UV-radiation emitted by the massive OB-stars, the gas inside a sphere centred around the MW, called the Strömgren sphere, became ionized and prevented the formation of stars. Outside the Strömgren sphere molecular gas can exist, allowing the formation of stars only at an ample distance from the MW's centre. This period in the evolution of the Universe is called re-ionization. The potential to study re-ionization has been greatly accelerated due to the development of LOFAR (Low-Frequency Array), which the VUB is heavily involved with (Buitink et al., 2014).

Although the exact details depend on the particulars of the re-ionization process, it is no stretch to assume that only a few subhaloes are massive enough and at a large enough distance to allow star formation. This explains why most subhaloes remain dark, while less massive sub-subhaloes are able to form stars. Since this scenario is somewhat comparable to that of the compact group of

dwarf galaxies, it reaps the same benefits. When the sub-subhaloes approach the MW's halo, tidal forces stretch the distribution in their plane of motion, while compressing it in the direction perpendicular to the plane. The coherent rotation, planar structure and presence in a semi-circle thus emerge naturally from N-body simulations, as is shown in Chapter 6.

# 5 N-BODY MODELS OF GALAXIES

In order to recreate Andromeda's plane of dwarfs by use of N-body simulations, two main components are needed. The first is an N-body code powerful enough to deal with simulations containing on the order of one million particles. All N-body simulations in this project were performed by use of the cosmological code GADGET-2. The code was set up to use a tree algorithm to update the phase space coordinates of the dark matter and stellar component, and smoothed particle hydrodynamics (SPH) for the gas particles. Since its name is an acronym for **GA**laxies with **D**ark matter and **G**as int**E**rac**T**, GADGET-2 is an ideal tool for simulating galactic interactions. It can run on all supercomputers as well as on desktop PCs and is freely available at http://www.mpa-garching.mpg.de/gadget/.

The second component is an input file for GADGET-2, containing the initial conditions of the simulation. N-body simulations adhere to the old addage, "garbage in, garbage out", thus the requirement for high quality initial conditions is absolute. To generate the position, velocity, mass and temperature (only for gas) for each particle, a combination of extra codes is needed. These codes were written in FORTRAN 90, due to its numerical speed and easily created binary files compatible with GADGET-2. This chapter discusses the model used to create a four component disk galaxy, comprising a dark matter halo, stellar bulge and both a stellar and gaseous disk.

## 5.1 USEFUL QUANTITIES

In the course of sampling the velocities of particles, it is often necessary to know the total enclosed mass $M(r)$, the density $\rho(r)$ or potential $\Phi(r)$ at a certain radius. To speed up calculations, a grid with logarithmic spacing is constructed ranging from $r = 10^{-3}$pc to $r = 10^{7}$pc. Starting from an analytic expression of the density, the total mass of a spherically symmetrical distribution can then be obtained by integrating equation (24a), which yields (24b)

$$\frac{dM}{dr} = 4\pi r^2 \rho(r)\,, \tag{24a}$$

$$M(r) = 4\pi \int \rho(r) r^2 dr\,. \tag{24b}$$

An array containing the value of the total enclosed mass at each grid point, can then easily be constructed by numerically evaluating equation (24b) at grid points. Using $M(r)$, the potential of a spherically symmetrical distribution then becomes

$$\Phi(r) = \int_r^\infty \frac{-GM(r)}{r^2} dr\,. \tag{25}$$

This quantity can thus be obtained by numerically integrating over all grid points. The escape velocity $v_{esc}$ of a particle is then defined as the velocity for which the kinetic energy equals the potential energy

$$v_{esc}(r) = \sqrt{|2 \cdot \Phi(r)|}\,. \tag{26}$$

## 5.2 GENERATING A DARK MATTER HALO

Though its existence has not been conclusively proven, observations of kinematics in spiral galaxies suggest that most of the mass resides in a dark matter halo. A spherically symmetric density profile that can be used to describe the dark matter haloes formed in cosmological simulations is the Navarro, Frenk and White (NFW) profile. Since the enclosed mass $M(r)$ inside radius $r$ of an NFW-profile becomes infinite as $r \to \infty$, the density function $\rho(r)$ is replaced by an exponential cut-off at large radii and thus becomes

$$\rho(r) = \begin{cases} \frac{\rho_s}{(r/r_s)[1+r/r_s]^2} & \text{if } r \le r_{vir} \\ \frac{\rho_s}{(r/r_s)[1+r/r_s]^2} \left(\frac{r}{r_{vir}}\right)^{\epsilon} \exp\left(\frac{r_{vir}-r}{r_{decay}}\right) & \text{if } r \ge r_{vir} \end{cases} \tag{27}$$

where $r_{vir}$, $r_s$ and $r_{decay}$ are respectively the virial radius, scale radius and decay radius (Kazantzidis et al., 2004, p. 38). Here, $r_{decay}$ is set equal to $r_{vir}$, which is a standard choice. To ensure continuity of the first derivative, $\epsilon$ (not to be confused with the softening length) is set equal to

$$\epsilon = -\frac{1+3(r_{vir}/r_s)}{1+r_{vir}/r_s} + 1 \,. \tag{28}$$

### 5.2.1 *Sampling positions*

The position of halo particles can then easily be sampled in spherical coordinates $(r, \theta, \phi)$. To obtain a spherically symmetrical halo, $\cos(\theta)$ and $\phi$ are sampled from a uniform distribution function (UDF) in the respective intervals $[-1, 1]$ and $[0, 2\pi]$. Calculating the enclosed mass corresponding to the density of equation (27) over a logarithmically spaced grid of $[10^{-3} pc, 10^{7} pc]$ is then done by numerical integration for $r \ge r_{vir}$ and by use of

$$M(r) = 4\pi\rho_0 r_s^3 \left[\ln\left(\frac{r_s + r}{r_s}\right) - \frac{r}{r_s + r}\right] \tag{29}$$

for $r < r_{vir}$ (Binney and Tremaine, 2011, p. 71). Creating an array that contains $\frac{M(r)}{M_{total}}$ for all corresponding grid point then yields a numerical cumulative distribution function for the radius of a particle. A value of $r$ can now be obtained by sampling a number from a UDF between $[0, 1]$, finding the indices of the cumulative distribution enclosing this value and finally, interpolating the value of $r$ from the grid. The random number thus corresponds to a shell of mass. While all shell percentiles are equally likely, the shells are not evenly spaced in radius. This method results in the correct number of particles in each shell, as defined by the given mass distribution.

### 5.2.2 *Sampling velocities*

The velocities of the particles can be sampled by use of an energy distribution function $f(E)$, which is obtained as a solution to the collisionless Boltzmann equation. While a more straightforward way would be to sample velocities using the velocity dispersion found from the Jeans equation, the assumption is then made that the distribution of velocities is Gaussian. Since this is often a poor approximation (Kazantzidis et al., 2004), velocities for the halo will be sampled by determining $f(E)$ and then applying the acceptance-rejection technique (Press, 1996). For a halo in equilibrium with isotropic velocities, the energy distribution function is

$$f(E) = \frac{1}{\sqrt{8}\pi^2} \left[\int_E^0 \frac{d^2\rho}{d\Phi^2} \frac{d\Phi}{\sqrt{\Phi - E}}\right] , \tag{30}$$

where $\Phi$ is the total potential and $E$ is the total energy of the particle (Kazantzidis et al., 2004, p. 38). Equation (30) can be calculated explicitly for the mass density profile of the halo (see Section D.1). Once a particle's position has been sampled, the distribution function gives us the probability of velocities. Therefore, the particle's velocity can be sampled.

As shown above, it is straightforward to sample a particle's radius, which in turn defines its local potential $\Phi(r)$ (equation (25)) and thus the local escape velocity (equation (26)). The velocity of a particle is then sampled by setting $v_i$ ($i \in \{x, y, z\}$) equal to the local escape velocity $v_{esc}$, multiplied by a random number sampled from a UDF between $[-1, 1]$. This set of velocities is temporarily accepted if the total velocity $v$ is smaller than the escape velocity. The energy $E = \Phi(r) + \frac{v^2}{2}$ corresponding to that velocity $v$ defines the local value $f(E)$ of the energy distribution function, as shown in figure 6. In this plot, the minimal value of $E$ is set by $\Phi(r)$. This is the energy the particle would have if it was stationary. Two other possible sampled velocities are shown, one with a high velocity (blue circle) and one with a lower velocity (purple circle). The probability of whether or not we accept these sampled velocities is given by the ratio of $\frac{f(E)}{f(\Phi(r))}$. In practice, this means we accept the velocities if $\frac{f(E)}{f(\Phi(r))}$ is larger than a random number from a UDF in $[0, 1]$. Lower velocities will thus be accepted more often than high velocities, as can be seen from the figure.

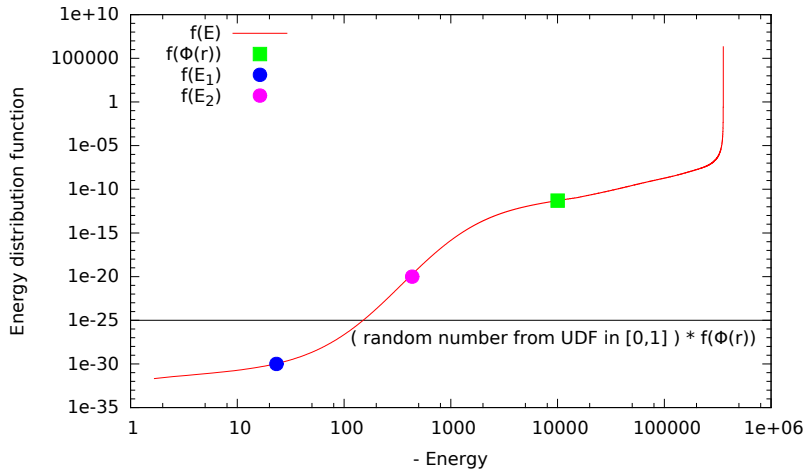


Figure 6: Graphical representation of the method used to sample the energy of particles in the halo. An energy $E = \Phi(r) + \frac{v^2}{2}$ is accepted if $\frac{f(E)}{f(\Phi(r))}$ is larger than a random number from a UDF in $[0, 1]$ (horizontal line). In this figure, $E_2$ (pink) would be accepted, while $E_1$ (blue) will be rejected.

## 5.3 GENERATING A STELLAR BULGE

A second major component of disk galaxies is the bulge. This central concentration of stars will, like the halo, be modelled by a spherically symmetric distribution function. When generating positions of particles in the bulge, the only difference with respect to the halo resides in obtaining $r$ from $\rho(r)$. The density profile used is

$$\rho(r) = \frac{M}{2\pi} \frac{a}{r} \frac{1}{(r+a)^3} , \tag{31}$$

where $a$ is a scale length and $M$ the total mass (Hernquist, 1990, p. 359). This profile has been used for decades to fit the luminosity of bulges.

### 5.3.1 *Sampling positions*

Making use of equation (24b), the total mass inside radius $r$ is

$$M(r) = M\frac{r^2}{(r+a)^2} \tag{32a}$$

$$r = \frac{a\sqrt{y}}{1-\sqrt{y}} \quad ; \quad y = \frac{M(r)}{M} \tag{32b}$$

Equation (32b) is equivalent to (32a), but gives an explicit formula for $r$. The radius of particles in the bulge can now be obtained by sampling $y$ as a random number from a UDF between $[0,1]$.

### 5.3.2 *Sampling velocities*

Once the radius is determined, the particle velocities can be obtained by solving the Jeans equation for a non-rotating spherically symmetric system

$$\frac{1}{\rho}\frac{d}{dr}\left(\rho\overline{v_r^2}\right) + 2\beta\frac{\overline{v_r^2}}{r} = -\frac{d\Phi}{dr}\ , \tag{33}$$

where $\beta(r) = 1 - \overline{v_\theta^2}/\overline{v_r^2}$ is the velocity anisotropy function and $\Phi$ is the total potential (Hernquist, 1990, p. 359). Considering a system with isotropic velocities ($\beta = 0$), the Jeans equation becomes (34a), which can then be solved for $\overline{v_r^2}(r)$ yielding (34b)

$$\frac{d}{dr}\left(\rho\overline{v_r^2}\right) = -\rho(r)\frac{d\Phi}{dr} \tag{34a}$$

$$\overline{v_r^2}(r) = \frac{1}{\rho(r)}\int_r^\infty \rho(r')\frac{d\Phi}{dr'}dr'\ . \tag{34b}$$

Since $\frac{d\Phi}{dr}$ is equal to the total gravitational force exerted on a particle of unit mass, it can be written as the sum of contributions from the halo, bulge and disks. Due to the spherical symmetry of both the halo and bulge, the gravitational force they exert equals

$$\frac{d\Phi_i}{dr} = -\frac{GM_i(r)}{r^2}\ . \tag{35}$$

As a first order approximation, equation (35) can also be used to describe the potential due to the disks. Calculating the exact form of $\frac{d\Phi_i}{dr}$ for the disks would result in an expression that is no longer solely dependent on $r$, which in return yields an anisotropic velocity dispersion.

Assuming we know the gravitational fields of the four mass components, the integral in equation (34b) can be numerically evaluated and solved on a grid. Values of $\overline{v_r^2}(r)$ are then obtained by interpolation, from which the velocity component of a particle $v_i$ ($i \in \{r,\theta,\phi\}$) can be sampled as a random number from a standard Gaussian distribution times $\sqrt{\overline{v_r^2}}$.

## 5.4 GENERATING A STELLAR AND GASEOUS DISK

### 5.4.1 *Stellar disk*

Observations have shown that the density profile of galactic disks can be well approximated by the product of two exponential distributions. If the disk is parallel to the $xy$-plane, the density profile equals

$$\rho(R,z) = \frac{M}{4\pi h^2 z_0} \exp\left(\frac{-R}{h}\right) \exp\left(\frac{-|z|}{z_0}\right), \tag{36}$$

where M is the total disk mass, $h$ and $z_0$ are the radial scale length and vertical scale height and $R$ is the radius in the $xy$-plane (Hernquist, 1993, p. 389).

#### 5.4.1.1 *Sampling positions*

The position of a particle can then be sampled in cylindrical coordinates $(R,\phi,z)$. Due to the azimuthal symmetry of the plane, $\phi$ can be chosen from a UDF between $[0,2\pi]$. Integrating equation (36) over all $\phi$, all $R$ and from $|z'| = 0$ to $|z'| = z$ yields the cumulative mass distribution in the $z$ direction (37a), which can be solved for $|z|$

$$M(z) = 2\pi \int_0^\infty dR \int_{-z}^{z} R\rho(R,z')dz' = M\left[1 - \exp\left(\frac{-|z|}{z_0}\right)\right] \tag{37a}$$

$$|z| = z_0 \ln\left(\frac{M}{M - M(z)}\right). \tag{37b}$$

Sampling $\frac{M(z)}{M}$ from a UDF between $[0,1]$ then generates a value of $|z|$, which is set equal to either $z$ or $-z$ with equal probability. Obtaining the enclosed mass distribution as a function of radius can be done similarly, by integrating equation (36) over all $\phi$, all $z$ and from $R = 0$ to $R = R'$

$$\begin{aligned} M(R) &= 2\pi \int_{-\infty}^{\infty} dz \int_{R'=0}^{R'=R} R'\rho(R',z)dR' \\ &= M \exp\left[1 - \exp\left(-\frac{R}{h}\right)\left(1 + \frac{R}{h}\right)\right]. \end{aligned} \tag{38}$$

Integrating numerically over a grid of $R$ then creates an array $\frac{M(R)}{M}$ that corresponds to the cumulative distribution function of $R$. Values can then be sampled in the usual way, by interpolating the $R$ that corresponds to a random number from a UDF in $[0,1]$.

#### 5.4.1.2 *Sampling velocities*

To sample the velocity of disk particles, a number of variables have to be calculated, including both the angular frequency $\Omega$ (Binney and Tremaine, 2011, p. 165) and the epicyclic frequency $\kappa$ (Hernquist, 1993, p. 392). These quantities can be derived from the total potential $\Phi$ as

$$\Omega^2(R) = \frac{1}{R}\left(\frac{\partial\Phi}{\partial R}\right), \tag{39a}$$

$$\kappa^2(R) = \frac{3}{R}\frac{\partial\Phi}{\partial R} + \frac{\partial^2\Phi}{\partial R^2}. \tag{39b}$$

Since $\Phi$ represents the total potential, $\frac{\partial\Phi}{\partial R}$ and its derivative with respect to $R$ can be written as the sum of contributions from the halo, bulge and disks. Explicit expressions for these quantities are derived and presented in Section D.2.

The vertical velocity dispersion $\overline{v_z^2}$ of a disk with an exponential vertical distribution can be approximated (van der Kruit, 1988; Bottema, 1993) as

$$\overline{v_z^2} = 1.5\pi G z_0 \Sigma(R) \,, \tag{40}$$

where $\Sigma(R)$ is the total surface density at radius $R$. An expression for $\Sigma(R)$ can be obtained by integrating equation (36) over all $z$. The result of this integration can be written as

$$\Sigma(R) = \exp\left(\frac{-R}{h}\right)\Sigma_0 \,. \tag{41}$$

Observations suggest that $\overline{v_R^2}$ is proportional to the disk's surface density as well and can thus be written as $\overline{v_R^2} = \alpha\overline{v_z^2}$ (Hernquist, 1993, p. 392). For disk galaxies that have a flat rotation curve, the dimensionless constant $\alpha$ is equal to 0.71 (Block et al., 2010, p. 155). What is left to calculate is the remaining component of the velocity dispersion $\sigma_\phi^2$. Unlike in the $R$ and $z$ direction, the average velocity in the azimuthal direction $\overline{v_\phi}$ is not equal to zero, because the disk is rotating. Random velocities in the $\phi$ direction that are added on top of the average rotation velocity therefore have to be sampled from a Gaussian with dispersion $\sigma_\phi^2$, which can be determined from the epicyclic approximation

$$\sigma_\phi^2 = \overline{v_R^2}\frac{\kappa^2}{4\Omega^2} \quad (\textit{Hernquist}, 1993, p.\ 392). \tag{42}$$

The only quantity that remains to be calculated is $\overline{v_\phi}$, which can be obtained from the second moment of the collisionless Boltzmann equation for an exponential disk

$$\overline{v_\phi}^2 - R\frac{\partial\Phi_{tot}}{\partial r} = \overline{v_r^2}\left(1 - \frac{\kappa^2}{4\Omega^2} - 2\frac{R}{h}\right) \quad (\textit{Hernquist}, 1993, p.\ 392). \tag{43}$$

Solving (43) for $\overline{v_\phi}$ trivially yields

$$\overline{v_\phi} = \sqrt{\overline{v_r^2}\left(1 - \frac{\kappa^2}{4\Omega^2} - 2\frac{R}{h}\right) + R\frac{\partial\Phi_{tot}}{\partial r}} \tag{44}$$

The particle velocities now becomes $v_R = a\overline{v_R^2}$, $v_\phi = \overline{v_\phi} + b\sigma_\phi^2$ & $v_z = c\overline{v_z^2}$, where $a$, $b$ & $c$ are random numbers sampled from a standard normal distribution.

### 5.4.2 *Gaseous disk*

Observing $\rho(z)$ of a gas disk is a difficult task, both due to the thinness of the disk and the low angular resolution of standard radio telescopes compared to optical telescopes. Modelling $\rho(z)$ using an exponential profile as in equation (36), appears to be a satisfactory approximation that is consistent with observations (Agertz et al., 2009, p. 296). For the radial direction, an exponential distribution is assumed as per the stellar disk. This is chosen for simplicity, since the true gas distributions of disk galaxies are highly irregular. Sampling positions for particles in the gas disk can thus be done as per the stellar disk, though parameters such as scale height might differ.

Unlike the stellar disk, particle forces other than gravity are this time modelled using smoothed particle hydrodynamics. Since the interaction between the gas particles damps any random velocity component, the velocity given to

each particle no longer requires a random component and is set equal to the circular velocity $v_c = \sqrt{R \frac{\partial \Phi_{tot}}{\partial R}}$ at $z = 0$. A graphical representation of the contribution of each component to $v_c$ is given in figure 7. Though the circular velocity is not independent of $z$, this approximation is justifiable due to the thinness of the gas disk (Wang et al., 2010, p. 705). Each particle is now given an internal energy equal to $\frac{3}{2}\overline{v_z^2}$ (units $\frac{km^2}{s^2}$, cf. with GADGET2 (Springel, 2014)), as defined in equation (40).

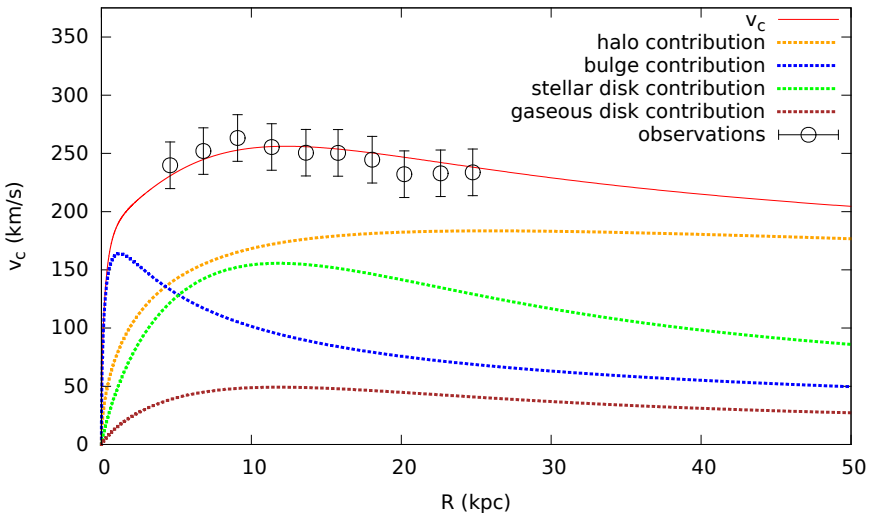


Figure 7: Dependency of the circular velocity $v_c$ on the radius $R$ in the $xy$-plane. The contribution of each of the four components to $v_c$ is represented by a dotted line. In addition to these quantities that define the model of M31, the data points represent measurements of the total circular velocity from radio observations (Widrow and Dubinski, 2005).

## 5.5 VERIFYING THE SYSTEM'S STABILITY

By generating initial conditions for a four component galaxy as described in the previous sections, the stability of the model can be tested by advancing a simulation of M31 over 5 Gyr. Ideally, the density and energy of each component should stay constant, since they are sampled to be in a state of equilibrium. The various approximations used to create the initial conditions however insure the existence of small instabilities, that are to be expected initially. When advancing the simulation, these instabilities are expected to settle down and turn into small fluctuations. The goal therefore is to generate a model for which the density profiles remain as close as possible to the theoretical profiles from which the components were sampled. To test if our model exhibits this kind of behaviour, the evolution of the cumulative distribution function of each component and total kinetic and potential energy were plotted as a function of time in figure 8 and 9.

The simulation was carried out in isolation using $4.22 \cdot 10^5$ particles, where each particle has equal mass. Variables such as the mass of each component were chosen to be representative for the Andromeda galaxy. Figure 8 shows that the total kinetic and potential energy undergo a change of around 6.6% and $-2.8\%$ respectively, after which they start fluctuating around a central value. Their ratio equals $\frac{E_{kin}}{E_{pot}} = 0.484$ initially and $\frac{E_{kin}}{E_{pot}} = 0.500$ at the end of

the simulation. The system therefore converges to a state of virial equilibrium. Furthermore, the evolution of the density of the halo, bulge and stellar disk exhibits a small change after a period of 5 Gyr. The component exhibiting the largest changes is the gaseous disk, which develops a higher central concentration and shows flaring for high $R$, as visible in figures 10 and 11.

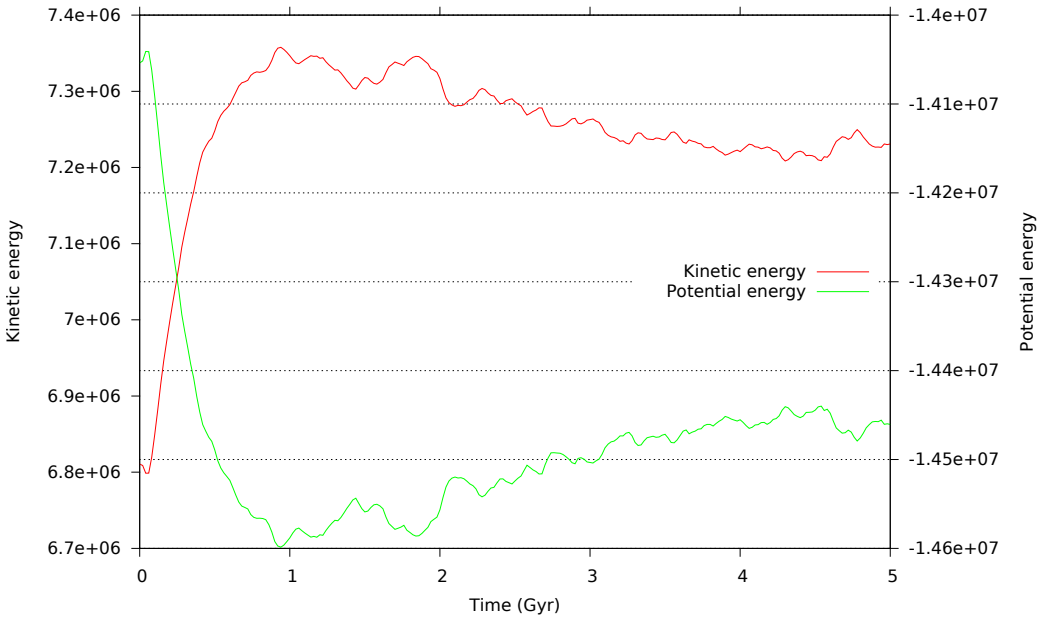


Figure 8: Evolution of the energy over 5 Gyr.

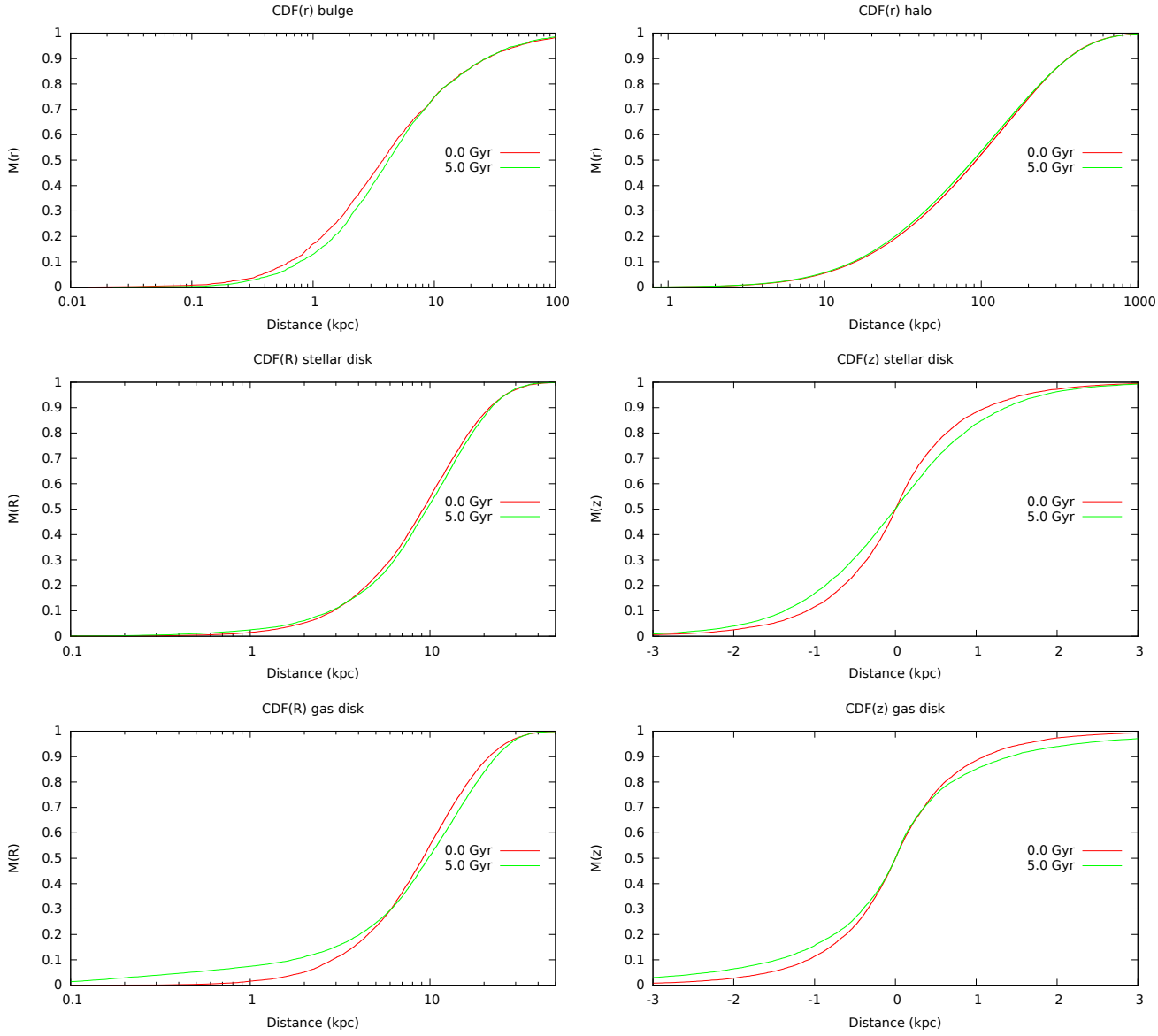


Figure 9: Evolution of the density over 5 Gyr.

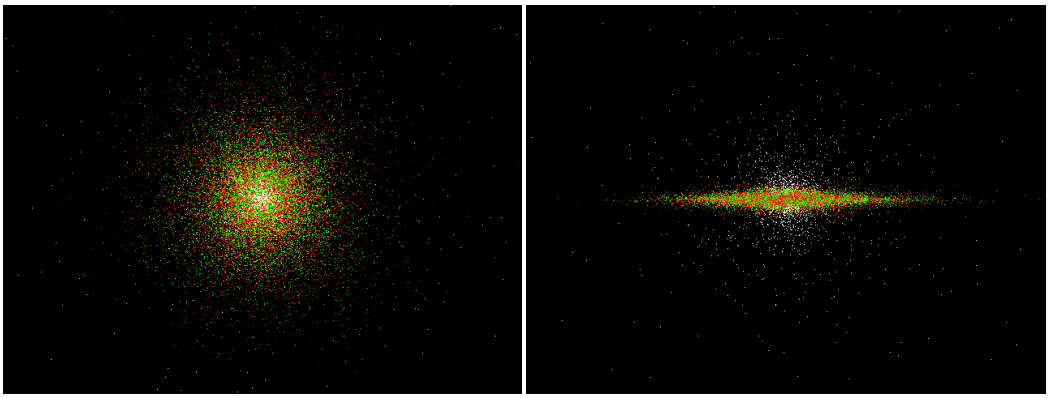

Figure 10: Initial distribution of the stellar disk (green dots), gaseous disk (red dots) and bulge (white dots).

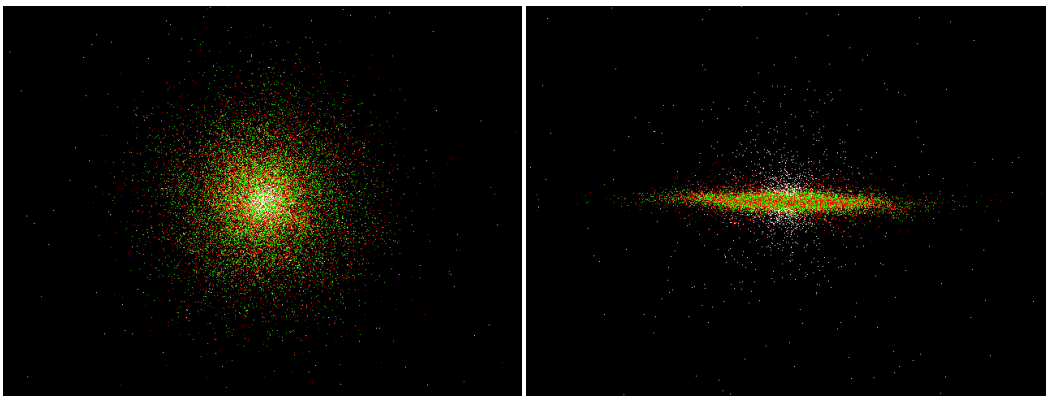

Figure 11: Distribution after 5 Gyr of the stellar disk (green dots), gaseous disk (red dots) and bulge (white dots).

# 6 SIMULATING M31'S PLANE OF DWARFS

Using the tools provided in Chapter 5, the interaction between M31 and M32 can now be simulated. The initial set-up of the simulation is based on the assumption that the dark matter halo of M32 corresponds to one of the most massive subhaloes of M31. dSph galaxies on the other hand, will be assumed to have an initial set-up that corresponds to the distribution of the dark matter sub-subhaloes around M32. Using current estimates for the variables describing M31 and M32 then allows the system to be simulated for different orbital parameters.

Each simulation was carried out on the VUB's HYDRA cluster using a total of 1.004.381 particles. The HYDRA cluster is a supercomputer comprising ~ 1200 cores and is available to all VUB employees. Since this project required the running of several similar simulations with modified parameters, the simulations used shared memory, thus multiple processors on a single node per simulation.

## 6.1 INITIAL SET-UP

Both M31 and M32 are set up as a four component galaxies that are initially separated by a distance of 450 $kpc$. The parameters used to generate the galaxies are based on Banerjee and Jog (2008); Widrow and Dubinski (2005); Dierickx et al. (2014) and are given in table 1.

| Component | Parameters | M31 | M32 |
|---|---|---|---|
| Halo | $\rho_s$ $(M_\odot/pc^3)$ | 0.02 | 0.001328 |
| | $r_s$ $(kpc)$ | 12.0 | 8.375 |
| | $r_{vir} = r_{decay}$ $(kpc)$ | 185 | 60.0 |
| Bulge | $M$ $(10^{10}\ M_\odot)$ | 3.0 | 0.032 |
| | $a$ $(kpc)$ | 1.2 | 0.25 |
| Stellar disk | $M$ $(10^{10}\ M_\odot)$ | 8.0 | 0.032 |
| | $h$ $(kpc)$ | 5.5 | 0.5 |
| | $z_0$ $(kpc)$ | 0.6875 | 0.0625 |
| Gaseous disk | $M$ $(10^{10}\ M_\odot)$ | 0.8 | 0.0032 |
| | $h$ $(kpc)$ | 5.5 | 0.5 |
| | $z_0$ $(kpc)$ | 0.15 | 0.15 |

Table 1: Variables describing M31 and M32

M31 was positioned at rest at the origin, with its disk parallel to the $xy$-plane. It was then rotated around the $y$-axis over an angle of 50.5°, so that the orientation of the disk with respect to the plane of dwarf galaxies is conform with observations (Pawlowski et al., 2013, p. 10). M32 was placed at ($x = 450\ kpc$, $y = 0\ kpc$, $z = 0\ kpc$) with its disk parallel to the $xy$-plane and an initial velocity $v$ in the $y$ direction. Ten simulations were carried out, in which

the size of $v$ correspondingly was $\{20, 25, 30, 35, 40, 45, 50, 55, 65, 80\}$ $(km/s)$.

Centred on M32, a system of 20.000 particles was added to represent the distribution of sub-subhaloes around M32. These particles were sampled using equation (23) with $c_2 = 0.81 \cdot r_{vir,M32}$, $\alpha = 0.678$ and $c_1$ determined by normalization (Springel et al., 2008, p. 1696). Since their density function $\rho(r)$ only depends on the distance to the centre of M32, positions and velocities could be sampled analogously to those of the bulge particles (described in Section 5.3). To ensure the stability of this system, a simulation was carried out with only M32 and the sub-subhalo particles. The evolution of the distribution of sub-subhaloes after a period of 5 Gyr is plotted in figure 12 and indicates the system is sampled close to equilibrium.

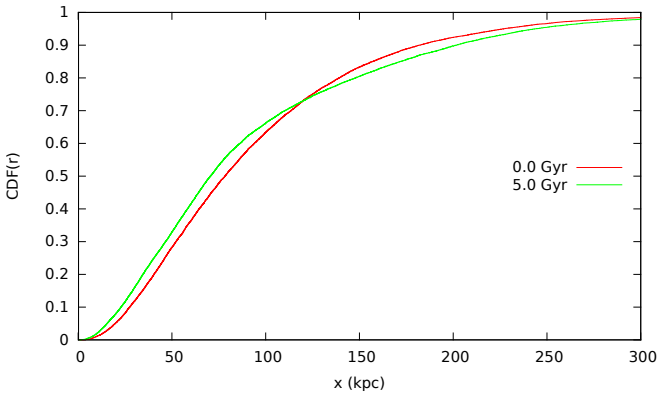


Figure 12: Evolution of the distribution of sub-subhaloes around M32 over 5 Gyr.

## 6.2 ANALYSIS

A total of 10 simulations were carried out, each with a different value for the initial velocity $v$ of M32. Since each value of $v$ is lower than the velocity needed to perform a circular orbit, M32 falls towards M31.

One of the toughest constraints on any model that aims to reproduce the planar distribution of the dSph galaxies, is that it must be as thin as the observed distribution. To determine whether the simulations are able to reproduce this feature, a Kolmogorov–Smirnov (KS) test was used to compare the cumulative distribution of dwarfs in the $z$ direction, with the simulated distribution of sub-subhaloes. For the dwarf galaxies, $\vec{1}_z$ corresponds to the direction perpendicular to the plane that minimizes the root-mean-square of the $z$-coordinate of the dwarfs. The sub-subhaloes on the other hand, are simulated in such a way that their plane of motion corresponds to the $xy$-plane. Their projected positions, as they would be observed from Earth, are then obtained by rotating the system around the $z$-axis, so that M32 lies directly in front of M31.

Based on Ibata et al. (2013), the dwarf galaxies used in the KS test are: And I, And III, And IX, And XI, And XII, And XIV, And XVI, And XVII, And XXV, And XXVI, NGC 147 and NGC 185. While And XIII and And XXVII lie in the planar subgroup as well, they do not belong to this sample since their velocity is inconsistent with the coherent rotation. They are therefore most likely galaxies of the non-planar subgroup, that by chance happen to lie close to the plane of the planar subgroup. Since observations covered an area out to a project distance

of 150 $kpc$ around M31, the cumulative distribution function of sub-subhaloes only counts the sub-subhaloes that lie inside the corresponding region.

The statistic of merit of a KS test is found from the maximal difference between the two cumulative distribution functions. Minimizing this difference optimizes the KS statistic. The simulations were therefore evaluated at the point in the orbit when the KS statistic is minimal, typically at or right after the closest approach of M32 around M31. The resulting values for each of the 10 simulations are shown in figure 13. For an initial velocity $v = 35\ km/s$ of M32, the KS statistic reaches a minimal value of 0.082. The corresponding cumulative distribution functions from which this value was derived are shown in figure 14. A graphical representation of this simulation is given in figure 15, 16 and 17.

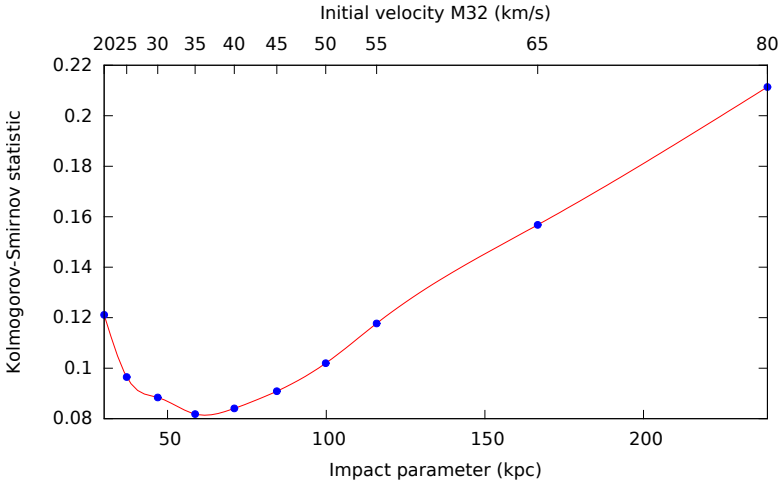


Figure 13: Minimal value of the KS statistic as a function of the initial velocity of M32 or the impact parameter between M32 and M31.

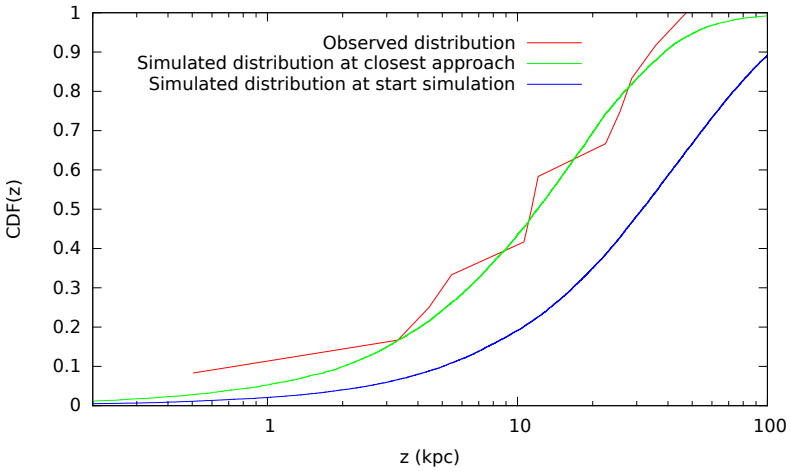


Figure 14: Cumulative distribution functions of the dwarf galaxies and sub-subhaloes for the simulation that minimizes the KS statistic. The blue and green lines respectively indicate the distribution of sub-subhaloes at the start of the simulation (KS statistic = 0.37) and when the KS statistic is minimal (0.082).

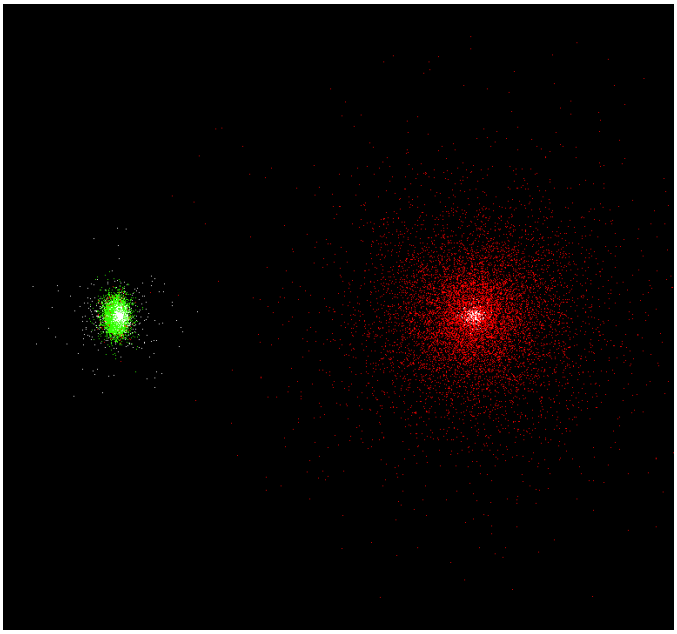

Figure 15: Initial distribution of the particles in the simulations. The galaxy on the left (green and white dots) is M31. To its right lies the distribution of sub-subhaloes (red dots), with at its centre M32 (moving upwards).

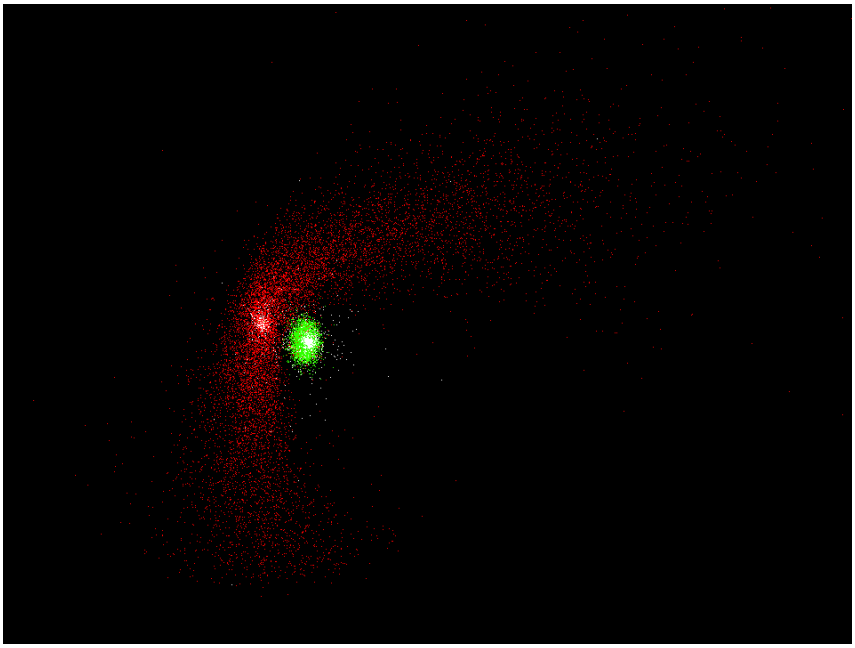

Figure 16: Distribution of sub-subhaloes (red dots) when the KS statistic is minimal. M32 now lies to the left of M31 (green and white dots) and is moving downwards.

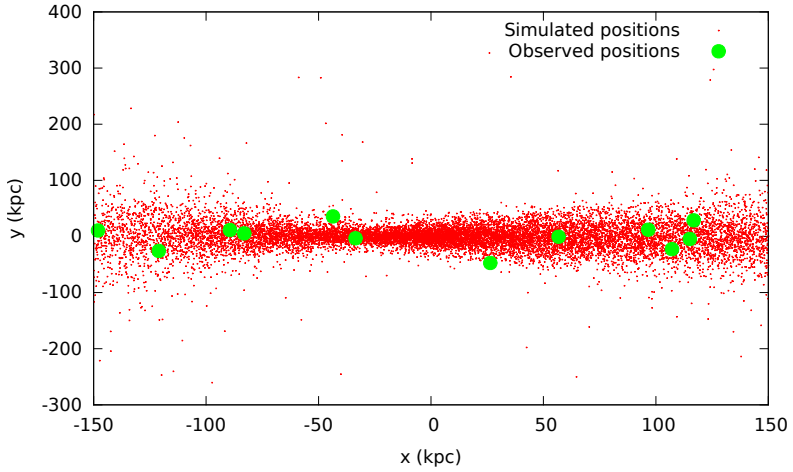


Figure 17: Simulated position of sub-subhaloes when the KS statistic is minimal, projected onto the plane of the sky (red dots). M32 lies directly in front of M31 at ($x = 0\ kpc, y = 0\ kpc$). For comparison, the observed positions of dSph galaxies belonging to the planar subgroup of M31 are plotted as well (green circles).

## 6.3 CONCLUSION

Simulations of the interaction between M32 and M31 have revealed that the simulated distribution of sub-subhaloes around M32 strongly resembles the observed positions of dSph galaxies belonging to the planar subgroup of M31. Applying a KS test between the two distributions yielded a value for the KS statistic of 0.082, which is much lower than the minimum value of 0.31 needed to prove the distributions are different at a significance of 80%. The simulations moreover recreated the coherent rotation and presence in a semi-circle as well and are thus in accordance with observations.

While the masses of most dSph galaxies in the planar subgroup are in agreement with the masses of the sub-subhaloes of M32, this is not the case for NGC 147 and NGC 185. A possible solution to this pickle is that they are subhaloes of M31, that became gravitationally bound to M32 during its fall towards M31. This is not an unprecedented scenario, since the LMC and SMC have become bound as they orbited towards the MW. Furthermore, NGC 147 and NCG 185 are already a binary pair. More advanced simulations will however be needed to model this kind of behaviour. This could be tackled by looking at the orbits of subhaloes in high resolution cosmological simulations, such as ELVIS (Exploring the Local Volume in Simulations ; Garrison-Kimmel et al. (2014)). The development of N-body codes that include extended gas physics (taking into account the effects of ionizing radiation, supernovae, ...) might moreover create simulations that explain the lighting up of dark matter (sub-)subhaloes.

In conclusion, a first step has been made in testing the validity of a theory that couples dark matter subhaloes of M32 to the planar subgroup of dwarf galaxies around M31. Simulations of the spatial distribution of sub-subhaloes have yielded a distribution that closely resembles the observed one. Further research is however needed to test this theory on the distribution of dwarfs around the MW and verify other aspects of the theory.

Part III

# APPENDIX

# A

# DIRECT GRAVITATIONAL N-BODY SIMULATIONS

## A.1 LEAPFROG ALGORITHM

### A.1.1 *Equivalent notations*

Subtracting equation (4a) from (5a), equation (45) is obtained

$$\dot{\vec{r}}_{i+1/2} = \dot{\vec{r}}_i + \frac{\Delta t}{2}\ddot{\vec{r}}_i. \tag{45}$$

This relation holds true for it is a first order Taylor expansion of $\dot{\vec{r}}$ and the Leapfrog algorithm is second order in $t$ for $\vec{r}$. This shows that in the second order expansion of $\vec{r}$, equation (4a) is equivalent to (5a). Subtracting equation (4b) from (5b) analogously yields a first order Taylor expansion of $\dot{\vec{r}}$, implying they are equivalent in second order of $\vec{r}$.

### A.1.2 *Time-reversibility of the equations*

The proof for the time-reversibility of the Leapfrog algorithm is given by use of equation (4a) and (4b). Time-reversibility implies that advancing $\vec{r}_i$ or $\dot{\vec{r}}_i$ by $\Delta t$ and $-\Delta t$ again yields $\vec{r}_i$. The proof of this relation is given by

$$\vec{r}_j = \vec{r}_{i+1} - \dot{\vec{r}}_{i+1/2}\cdot\Delta t = \left(\vec{r}_i + \dot{\vec{r}}_{i+1/2}\cdot\Delta t\right) - \dot{\vec{r}}_{i+1/2}\cdot\Delta t = \vec{r}_i \tag{46a}$$

$$\dot{\vec{r}}_j = \dot{\vec{r}}_{i+1} - \ddot{\vec{r}}_{i+1/2}\cdot\Delta t = \left(\dot{\vec{r}}_i + \ddot{\vec{r}}_{i+1/2}\cdot\Delta t\right) - \ddot{\vec{r}}_{i+1/2}\cdot\Delta t = \dot{\vec{r}}_i \tag{46b}$$

## A.2 HERMITE ALGORITHM

### A.2.1 *Updating the phase space coordinates*

The Hermite algorithm is a fourth order algorithm and thus uses higher order derivatives of $\vec{r}$ (Dehnen and Read, 2011, p. 6). To maintain readability, the variables velocity $\vec{v} = \frac{d\vec{r}}{dt}$, acceleration $\vec{a} = \frac{d^2\vec{r}}{dt^2}$, jerk $\vec{j} = \frac{d^3\vec{r}}{dt^3}$, snap $\vec{s} = \frac{d^4\vec{r}}{dt^4}$ and crackle $\vec{c} = \frac{d^5\vec{r}}{dt^5}$ are defined. Updating the phase space coordinates can be done using

$$\vec{r}_{i+1} = \vec{r}_i + \frac{\Delta t}{2}(\vec{v}_i + \vec{v}_{i+1}) + \frac{(\Delta t)^2}{12}(\vec{a}_i - \vec{a}_{i+1})\,, \tag{47a}$$

$$\vec{v}_{i+1} = \vec{v}_i + \frac{\Delta t}{2}(\vec{a}_i + \vec{a}_{i+1}) + \frac{(\Delta t)^2}{12}(\vec{j}_i - \vec{j}_{i+1})\,. \tag{47b}$$

Both equation (47a) and (47b) are derived in Section A.2.2. The jerk present in the updated velocity can be calculated by deriving equation (1b). Denoting quantities $\vec{x}_{ab}$ as the value of $\vec{x}$ from particle $b$ on $a$ and $\vec{x}_a$ as the total value of $\vec{x}$ on particle $a$, the jerk becomes

$$\vec{j}_b = G\sum_{a=1,a\neq b}^{N} M_a\left(\frac{\vec{v}_{ab}}{r_{ab}^3} - 3\frac{(\vec{r}_{ab}\cdot\vec{v}_{ab})\vec{r}_{ab}}{r_{ab}^5}\right) \tag{48}$$

Due to the dependence of $\vec{r}_{i+1}$ and $\vec{v}_{i+1}$ on $\vec{a}_{i+1}$ and $\vec{j}_{i+1}$, it is impossible to update the phase space coordinates using just equation (47a) and (47b). This quandary can be averted by using a Predict-Evaluate-Correct (PEC) scheme. The predicted value $\vec{r}_p$ and $\vec{v}_p$ are obtained by use of a Taylor expansion

$$\vec{r}_p = \vec{r}_i + \Delta t \cdot \vec{v}_i + \frac{(\Delta t)^2}{2}\vec{a}_i + \frac{(\Delta t)^3}{6}\vec{j}_i \,, \tag{49a}$$

$$\vec{v}_p = \vec{v}_i + \Delta t \cdot \vec{a}_i + \frac{(\Delta t)^2}{2}\vec{j}_i \,. \tag{49b}$$

These values can then be used to obtain estimates of $\vec{a}_{i+1}$ and $\vec{j}_{i+1}$, which in return can be inserted into equation (47b). Finally, the updated velocity and and estimates $\vec{a}_{i+1}$ can be inserted into equation (47a) to obtain the corrected value of $\vec{r}_{i+1}$. This method can be justified by noting that the predicted value $\vec{r}_p$ with error $\mathcal{O}(\Delta t^4)$ inserted in (47a) produces an error $\mathcal{O}(\Delta t^6)$ in $\vec{r}_{i+1}$. Since the Hermite algorithm is fourth order and thus has errors $\mathcal{O}(\Delta t^5)$, the PEC scheme is a valid approach. The error in $\vec{v}_{i+1}$ due the predicted values is likewise of smaller order than that of the algorithm.

In an analogous way to the Leapfrog algorithm, it is easily seen that the equations used to update the phase space coordinates are time-reversible. This combined with their short form and the elimination of $\vec{s}$, constitutes the main reasons for writing the algorithm by use of equation (47a) and (47b).

### A.2.2 *Derivation*

The derivation of equation (47a) and (47b) is based on Hut and Makino (2006) and can be realized by use of a fifth order Taylor-expansion of $\vec{r}$ in $t$

$$\vec{r}_{i+1} = \vec{r}_i + \vec{v}_i\Delta t + \frac{\vec{a}_i}{2}(\Delta t)^2 + \frac{\vec{j}_i}{6}(\Delta t)^3 + \frac{\vec{s}_i}{24}(\Delta t)^4 + \frac{\vec{c}_i}{120}(\Delta t)^5 \tag{50a}$$

$$\vec{v}_{i+1} = \vec{v}_i + \vec{a}_i\Delta t + \frac{\vec{j}_i}{2}(\Delta t)^2 + \frac{\vec{s}_i}{6}(\Delta t)^3 + \frac{\vec{c}_i}{24}(\Delta t)^4 \tag{50b}$$

$$\vec{a}_{i+1} = \vec{a}_i + \vec{j}_i\Delta t + \frac{\vec{s}_i}{2}(\Delta t)^2 + \frac{\vec{c}_i}{6} \tag{50c}$$

$$\vec{j}_{i+1} = \vec{j}_i + \vec{s}_i\Delta t + \frac{\vec{c}_i}{2}(\Delta t)^2 \,. \tag{50d}$$

By multiplying (49b) by $\Delta t$ and subtracting respectively 2 and 3 times equation (50c), equation (50c) and (50d) can be solved for the snap and crackle

$$\vec{s}_i = 6(\vec{a}_{i+1} - \vec{a}_i)(\Delta t)^{-2} - 2(\vec{j}_{i+1} + 2\vec{j}_i)(\Delta t)^{-1} \tag{51a}$$

$$\vec{c}_i = -12(\vec{a}_{i+1} - \vec{a}_i)(\Delta t)^{-3} + 6(\vec{j}_{i+1} + 2\vec{j}_i)(\Delta t)^{-2} \,. \tag{51b}$$

Inserting both equation (51a) and (51b) into (50a) and (50b) returns

$$\vec{r}_{i+1} = \vec{r}_i + \vec{v}_i\Delta t + \left(\frac{7}{20}\vec{a}_i + \frac{3}{20}\vec{a}_{i+1}\right)(\Delta t)^2 + \left(\frac{1}{20}\vec{j}_i - \frac{1}{30}\vec{j}_{i+1}\right)(\Delta t)^3 \tag{52a}$$

$$\vec{v}_{i+1} = \vec{v}_i + \frac{\Delta t}{2}(\vec{a}_i + \vec{a}_{i+1}) + \frac{(\Delta t)^2}{12}(\vec{j}_i - \vec{j}_{i+1}) \,. \tag{52b}$$

The validity of equation (47b) is thereby proven. The factor $\vec{v}_i$ in equation (52a) can be written as $2(\vec{v}_i/2 + \vec{v}_i/2)$. Replacing one of these factors with the expression obtained by solving equation (52b) for $\vec{v}_i$ gives

$$\vec{r}_{i+1} = \vec{r}_i + \frac{1}{2}(\vec{v}_i + \vec{v}_{i+1})\Delta t + \frac{1}{10}(\vec{a}_i - \vec{a}_{i+1})(\Delta t)^2 + \frac{1}{120}(\vec{j}_i + \vec{j}_{i+1})(\Delta t)^3 \,. \tag{53}$$

By inserting respectively a second and first order Taylor-expansion of $\vec{a}_{i+1}$ and $\vec{j}_{i+1}$ into (53) (both these Taylor-expansion are conform with a fourth order Taylor expansion of $\vec{r}$ in $t$), the resulting formula (54) is recovered

$$\vec{r}_{i+1} = \vec{r}_i + \frac{1}{2}(\vec{v}_i + \vec{v}_{i+1})\Delta t - \frac{1}{12}\vec{j}_i(\Delta t)^3 - \frac{1}{24}\vec{s}_i(\Delta t)^4 \ . \tag{54}$$

This result proves the validity of equation (47b) for its equivalency can by shown by writing $\vec{a}_{i+1}$ as a second order Taylor-expansion and noting that

$$\begin{aligned} \frac{1}{12}(\vec{a}_i - \vec{a}_{i+1})(\Delta t)^2 &= \frac{(\Delta t)^2}{12}\left(\vec{a}_i - \left(\vec{a}_i + \vec{j}_i\Delta t + \frac{1}{2}\vec{s}_i(\Delta t)^2\right)\right) \\ &= -\frac{1}{12}\vec{j}_i(\Delta t)^3 - \frac{1}{24}\vec{s}_i(\Delta t)^4 \ . \end{aligned} \tag{55}$$

# B

# APPROXIMATION SCHEMES

## B.1 APPEL'S SCHEME

Appel's tree algorithm is analogous to that of Barnes-Hut, but uses a different tree structure known as a k-d tree. One of the main differences between the two algorithms, is that Appel's scheme by design combines particles that are close together into a cell. The k-d tree is built by creating a clump that surrounds all particles. This clump is split into two subclumps, containing respectively all particles with $x$ coordinates smaller or larger than the *median* $x$ coordinate. These subclumps are then divided analogously using the $y$, and after that, the $z$ coordinate. This process is then repeated by iteration until subclumps contain one particle (Appel, 1985, p. 99).

The construction of the tree only happens once per simulation. After each time step, the tree is updated by adjustments known as grabs. During this procedure, the algorithm finds the closest clump $C'$ to a certain clump $C$. If $C$ was previously clumped together with $D$, but $C'$ is closer to $C$ than $D$, then both $C$ and $C'$ will be grouped together and clumped with $D$. A visualization of this technique is given in figure 18 (Appel, 1985, p. 97).

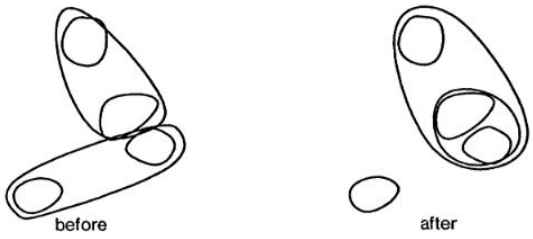


Figure 18: Demonstration of the appel grabs procedure that is used to update the structure of a k-d tree (Appel, 1985, p. 97).

Even though a standard k-d tree might initially separate particles that are close-by, after tree iterations the grab procedure has already resolved this issue (Appel, 1985, p. 99). Though the tree doesn't have to be rebuild at each time step, Appel's algorithm does require more force computations than the Barnes-Hut algorithm. Forces two particles exert on each other are however equal and opposite (Sellwood, 1987, p. 179).

## B.2 ALLOCATING MASS TO GRID CELLS

And example of a second order interpolation algorithm is the triangular shaped clouds (TSC) method. A graphical representation of TSC in one dimension is given in figure 19, where the amount of mass allocated to grid cell $x_p$ is proportional to the surface of $S$ in that interval. The advantage of using a higher order algorithm is obvious in that whereas the NGP method yields a discontinuous density field (when a particle shifts from one grid cell to another), the CIC method produces a force that is linear and continuous. Its first derivative is however discontinuous in contrast with the higher order TSC method. The

use of higher order algorithms does nonetheless increase the computational cost, making the CIC and TSC method popular choices (Springel, 2014, p. 24).

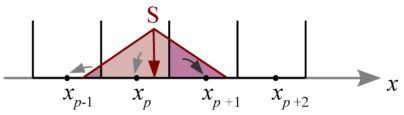


Figure 19: Distribution of mass over grid cells obtained when using the TSC method in one dimension (Springel, 2014, p. 24).

## B.3 APPROXIMATING DISCRETE DIFFERENTIALS

The discrete differential of $\Phi$ in a grid with spacing $d$ can be calculated by use of

$$\frac{\partial \Phi}{\partial x} = \sum_{\alpha=-4}^{4} \frac{\beta_\alpha \Phi_{i+\alpha,j,k}}{d}. \tag{56}$$

A list giving the coefficients $\beta_\alpha$ of $\Phi_{i+\alpha,j,k}$ is given in figure 20, where $\alpha$ corresponds to the different $x$ coordinates of the surrounding nodes. The order of accuracy $\gamma$ denotes the order $\mathcal{O}(d^\gamma)$ to which the error is proportional.

| Order of derivative | Order of accuracy | Approximations at $x = 0$; $x$-coordinates at nodes: −4 | −3 | −2 | −1 | 0 | 1 | 2 | 3 | 4 |
|---|---|---|---|---|---|---|---|---|---|---|
| **0** | ∞ | | | | | 1 | | | | |
| **1** | 2 | | | | $\frac{-1}{2}$ | 0 | $\frac{1}{2}$ | | | |
| | 4 | | | $\frac{1}{12}$ | $\frac{-2}{3}$ | 0 | $\frac{2}{3}$ | $\frac{-1}{12}$ | | |
| | 6 | | $\frac{-1}{60}$ | $\frac{3}{20}$ | $\frac{-3}{4}$ | 0 | $\frac{3}{4}$ | $\frac{-3}{20}$ | $\frac{1}{60}$ | |
| | 8 | $\frac{1}{280}$ | $\frac{-4}{105}$ | $\frac{1}{5}$ | $\frac{-4}{5}$ | 0 | $\frac{4}{5}$ | $\frac{-1}{5}$ | $\frac{4}{105}$ | $\frac{-1}{280}$ |

Figure 20: Coefficients for discrete differentials (Fornberg, 1988, p. 702)

## B.4 CONSERVATION OF MOMENTUM

The total momentum is persevered when using grids only when there are no self-forces and particles exert equal and opposite forces on each other. The fact that a particle cannot exert a force on itself can be shown as follows.

Consider the acceleration at grid point $p$. Because the Fourier technique offers an exact solution for a given distribution of masses $m_{p'}$ at grid points $p'$, it follows that the potential at grid points depends linearly on the masses of surrounding grid points, as would be expected from the superposition principle. From equation (16) and (56), it follows that the acceleration also linearly depends on the masses of surrounding grid points and thus can be written as

$$\vec{a}_p = \sum_{p'} \vec{d}(p,p') m_{p'}, \tag{57}$$

where $\vec{d}$ is some function for which $\vec{d}(p,p') = -\vec{d}(p',p)$. The force a particle (of mass $m$ located at $\vec{x}$) would exert on itself $\vec{F}_s(\vec{x})$ can then be written as

$$\begin{aligned}\vec{F}_s(\vec{x}) &= m\vec{a}(\vec{x}) \\ &= m\sum_p W_p(\vec{x})\vec{a}_p \\ &= m\sum_p W_p(\vec{x})\sum_{p'}\vec{d}(p,p')m_{p'} \\ &= m\sum_p W_p(\vec{x})\sum_{p'}\vec{d}(p,p')mW_{p'}(\vec{x}) \\ &= m^2\sum_{p,p'} W_p(\vec{x})W_{p'}(\vec{x})\vec{d}(p,p') \\ &= 0.\end{aligned} \tag{58}$$

This calculated was done by first substituting $\vec{a}(\vec{x})$ by use of equation (17), then replacing $\vec{a}_p$ by use of equation (57), then only considering the contribution from the particle itself and finally using $\vec{d}(p,p') = -\vec{d}(p',p)$ (Springel, 2014, p. 27).

By making the exact same substitutions as in equation (58), the force $\vec{F}_{12}$ exerted by particle 1 on particle 2 can be written as

$$\vec{F}_{12} = m_1 m_2 \sum_{p,p'} W_p(\vec{x}_1)W_{p'}(\vec{x}_2)\vec{d}(p,p'). \tag{59}$$

In the same way, the force $\vec{F}_{21}$ exerted by particle 2 on particle 1 equals

$$\vec{F}_{21} = m_2 m_1 \sum_{q,q'} W_q(\vec{x}_2)W_{q'}(\vec{x}_1)\vec{d}(q,q'). \tag{60}$$

Since both equation (59) and (60) sum $p,p',q$ and $q'$ over all grid points, it is possible to choose $q = p'$ and $q' = p$. Again, using $\vec{d}(p,p') = -\vec{d}(p',p)$ allows to rewrite equation (60) as

$$\begin{aligned}\vec{F}_{21} &= -m_1 m_2 \sum_{p,p'} W_p(\vec{x}_2)W_{p'}(\vec{x}_1)\vec{d}(p,p') \\ &= -\vec{F}_{12} \quad (Springel, 2014, p. 27).\end{aligned} \tag{61}$$

One way of determining the optimal value of the softening length $\epsilon$, is by choosing it so that it minimizes the Mean Integrated Square Error (MISE) of the force. This function is defined as

$$MISE(\epsilon) = \mathbb{E}\left[\int \rho(r)|\vec{F}(\vec{r},\epsilon) - \vec{F}_{true}(\vec{r})|^2 d\vec{r}\right] , \tag{62}$$

where $\mathbb{E}$ denotes that the average is taken over different configurations of the system, $\vec{F}(\vec{r},\epsilon)$ is the softened force on a particle at position $\vec{r}$ due to $N$ particles and $\vec{F}_{true}$ is the force due to the continuous distribution function based on which the $N$ particles were sampled (Zhan, 2006, p. 1). Numerical simulations of the MISE for the Hernquist and Plummer distribution have shown that the softening length should optimally be 1.5 to 2 times smaller than the mean distance between particles in the most dens region. In addition, a time step should be chosen such that the average distance traversed per time step is smaller than $\epsilon/2$ (Rodionov and Sotnikova, 2005, p. 11).

# D

# N-BODY MODELS OF GALAXIES

## D.1 ENERGY DISTRIBUTION FUNCTION OF THE HALO

Since the integration in equation (30) is carried out numerically, the only remaining difficulty when calculating the energy distribution of the halo lies in obtaining an expression for $\frac{d^2\rho}{d\psi^2}$, where $\Phi = -\psi$. For variables that are only a function of $r$, it is possible to write

$$\frac{d}{d\psi} = \frac{d}{dr}\frac{dr}{d\psi} \,. \tag{63}$$

Applying this trick twice for $\rho$ yields

$$\frac{d^2\rho}{d\psi^2} = \frac{d^2\rho}{dr^2}\left(\frac{dr}{d\psi}\right)^2 + \frac{d\rho}{dr}\frac{d^2r}{d\psi^2} \,. \tag{64}$$

It now remains to calculate both $\frac{dr}{d\psi}$ and $\frac{d^2r}{d\psi^2}$. This first quantity is minus the inverse of the gravitational force per unit mass, from which it follows that

$$\frac{dr}{d\psi} = \frac{r^2}{GM(r)} \,. \tag{65}$$

The second quantity can now be obtained by applying (63) to equation (65). The resulting formula is

$$\frac{d^2r}{d\psi^2} = \frac{2rGM(r) - r^2G\frac{dM}{dr}}{G^2M(r)^2} \cdot \frac{dr}{d\psi} \,, \tag{66}$$

For spherically symmetric mass distributions, $\frac{dM}{dr}$ can be obtained from equation (24a). The contribution from disk particles can be derived from equation (38), where the approximation is made that the mass inside a sphere of radius $r$ corresponds to the mass inside a cylinder of radius $r$. At larger radii, this thus becomes a better approximation. It would moreover be exact if the disk is infinitely thin. Combining everything finally yields

$$\frac{d^2\rho}{d\psi^2} = \left(\frac{r}{GM(r)}\right)^2 \left[r^2\left(\frac{d^2\rho}{dr^2}\right) + \left(\frac{d\rho}{dr}\right)\frac{2rM(r) - r^2\frac{dM}{dr}}{M(r)}\right] \,. \tag{67}$$

Setting $f(r = 10^7\ pc) = 0$ and inserting equation (67) into (30) then allows the integral to be calculated numerically for each grid point (Kazantzidis, 2003, p. 18).

## D.2 VELOCITIES OF DISK PARTICLES

Due to the spherical symmetry of the bulge and halo, their contributions to $\frac{\partial\Phi}{\partial R}$ have the same functional form. Writing the total radius as $r = \sqrt{R^2 + z^2}$ and $M$ for the total mass of the component under consideration, these expressions become

$$\begin{aligned} \frac{\partial\Phi_{h\&b}}{\partial R} &= \frac{\partial\Phi}{\partial r}\frac{\partial r}{\partial R} \\ &= \frac{GM}{r^2}\frac{R}{r} \\ &= GM\frac{R}{r^3} \,, \end{aligned} \tag{68}$$

$$\begin{aligned}\frac{\partial^2\Phi_{h\&b}}{\partial R^2} &= \frac{GM}{r^3} + GR\frac{\partial}{\partial r}\left(\frac{M}{r^3}\right)\frac{\partial r}{\partial R} \\ &= \frac{GM}{r^3} - 3GM\frac{R^2}{r^5} + G\frac{R^2}{r^4}\frac{\partial M}{\partial r} \ .\end{aligned} \tag{69}$$

Obtaining $\frac{\partial\Phi}{\partial R}$, and its derivative to $R$ for a disk is a bit more tricky. Denoting $y \equiv \frac{R}{2h}$, the first expression becomes

$$\begin{aligned}\frac{\partial\Phi_{disk}}{\partial R} &= 4\pi G\Sigma_0\frac{h}{R}y^2[I_0(y)K_0(y) - I_1(y)K_1(y)] \\ &= \frac{GMy}{h^2}[I_0(y)K_0(y) - I_1(y)K_1(y)] \ ,\end{aligned} \tag{70}$$

where $I_i$ and $K_i$ are modified Bessel functions and $\Sigma_0 = \frac{M_{gas}}{2\pi h_{gas}^2} + \frac{M_{stellar}}{2\pi h_{stellar}^2}$ is the total surface density at the centre of the disk (Binney and Tremaine, 2011, p. 101). Deriving equation (70) with respect to $R$ gives

$$\frac{\partial^2\Phi_{disk}}{\partial R^2} = \frac{GM}{2h^3}\left(I_0(y)K_0(y) + I_1(y)K_1(y) + \frac{R}{h}[I_1(y)K_0(y) - I_0(y)K_1(y)]\right) \ . \tag{71}$$

# BIBLIOGRAPHY


J. Adamek, D. Daverio, R. Durrer, and M. Kunz. General relativistic N-body simulations in the weak field limit. *Physical Review D*, 88(10):103527, November 2013. doi: 10.1103/PhysRevD.88.103527.

O. Agertz, G. Lake, R. Teyssier, B. Moore, L. Mayer, and A. B. Romeo. Large-scale galactic turbulence: can self-gravity drive the observed HI velocity dispersions? *Monthly Notices of the Royal Astronomical Society*, 392:294–308, January 2009. doi: 10.1111/j.1365-2966.2008.14043.x.

A. W. Appel. An Efficient Program for Many-Body Simulation. *Siam Journal on Scientific and Statistical Computing*, 6, 1985. doi: 10.1137/0906008.

J. S. Bagla. TreePM: A Code for Cosmological N-Body Simulations. *Journal of Astrophysics and Astronomy*, 23:185–196, December 2002. doi: 10.1007/BF02702282.

A. Banerjee and C. J. Jog. The Flattened Dark Matter Halo of M31 as Deduced from the Observed H I Scale Heights. *The Astrophysical Journal*, 685:254–260, September 2008. doi: 10.1086/591223.

J. Barnes and P. Hut. A hierarchical O(N log N) force-calculation algorithm. *Nature*, 324:446–449, December 1986. doi: 10.1038/324446a0.

J. Bers. M31: The andromeda galaxy. *Astronomy Picture of the Day*, 30 July 2014. URL http://apod.nasa.gov/apod/ap140730.html.

J. Binney and S. Tremaine. *Galactic Dynamics: (Second Edition): (Second Edition)*. Princeton Series in Astrophysics. Princeton University Press, 2011. ISBN 9781400828722.

D. L. Block, K. Freeman, and I. Puerari. *Galaxies and their Masks: A Conference in Honour of K.C. Freeman, FRS*. Springer New York, 2010. ISBN 9781441973177.

P. Bodenheimer, G.P. Laughlin, M. Rozyczka, T. Plewa, H.W. Yorke, and H.W. Yorke. *Numerical Methods in Astrophysics: An Introduction*. Series in Astronomy and Astrophysics. Taylor & Francis, 2006. ISBN 9780750308830.

R. Bottema. The Stellar Kinematics of Galactic Disks. *Astronomy & Astrophysics*, 275:16, August 1993.

M. Boylan-Kolchin, J. S. Bullock, and M. Kaplinghat. Too big to fail? The puzzling darkness of massive Milky Way subhaloes. *Monthly Notices of the Royal Astronomical Society*, 415:L40–L44, July 2011. doi: 10.1111/j.1745-3933.2011.01074.x.

M. Boylan-Kolchin, J. S. Bullock, and M. Kaplinghat. The Milky Way's bright satellites as an apparent failure of ΛCDM. *Monthly Notices of the Royal Astronomical Society*, 422:1203–1218, May 2012. doi: 10.1111/j.1365-2966.2012.20695.x.

B. Bryson. *A Short History of Nearly Everything*. Crown Publishing Group, 2003. ISBN 9780767916417.

S. Buitink, A. Corstanje, J. E. Enriquez, H. Falcke, J. R. Hörandel, T. Huege, A. Nelles, J. P. Rachen, P. Schellart, O. Scholten, S. ter Veen, S. Thoudam, and T. N. G. Trinh. Method for high precision reconstruction of air shower $X_{max}$ using two-dimensional radio intensity profiles. *Physical Review D: Particles, Fields, Gravitation & Cosmology*, 90(8):082003, October 2014. doi: 10.1103/PhysRevD.90.082003.

S. Carles. *European Congress of Mathematics*, volume 201 of *Progress in Mathematics*. Birkhauser Basel, 2001. doi: 10.1007/978-3-0348-8268-2_6.

A. Craps and C. Waelkens. Introduction to cosmology. Syllabus, VUB, 2013.

W. Dehnen and J. I. Read. N-body simulations of gravitational dynamics. *European Physical Journal Plus*, 126:55, May 2011. doi: 10.1140/epjp/i2011-11055-3.

M. Dierickx, L. Blecha, and A. Loeb. Signatures of the M31-M32 Galactic Collision. *The Astrophysical Journal, Letters*, 788:L38, June 2014. doi: 10.1088/2041-8205/788/2/L38.

E. D'Onghia and G. Lake. Small Dwarf Galaxies within Larger Dwarfs: Why Some Are Luminous while Most Go Dark. *The Astrophysical Journal, Letters*, 686:L61–L65, October 2008. doi: 10.1086/592995.

J. Dubinski. A parallel tree code. *New Astronomy*, 1:133, 1996. doi: 10.1016/S1384-1076(96)00009-7.

M. J. Duncan, H. F. Levison, and M. H. Lee. A Multiple Time Step Symplectic Algorithm for Integrating Close Encounters. *The Astronomical Journal*, 116:2067–2077, October 1998. doi: 10.1086/300541.

R. P. Feynman. *Surely You're Joking Mr Feynman: Adventures of a Curious Character as Told to Ralph Leighton*. Random House, 2014. ISBN 9781448181476.

B. Fornberg. Generation of Finite Difference Formulas on Arbitrarily Spaced Grids. *Mathematics of Computation*, 51(184):699–706, 1988. ISSN 00255718. doi: 10.2307/2008770.

S. Garrison-Kimmel, M. Boylan-Kolchin, J. S. Bullock, and K. Lee. ELVIS: Exploring the Local Volume in Simulations. *Monthly Notices of the Royal Astronomical Society*, 438:2578–2596, March 2014. doi: 10.1093/mnras/stt2377.

D. J. Griffiths. *Introduction to Electrodynamics (3rd Edition)*. Benjamin Cummings, 1998. ISBN 9780138053260.

H. Hayes. Efficient shadowing of high dimensional chaotic systems with the large astrophysical n-body problem as an example. master thesis, University of Toronto, January 1995.

L. Hernquist. An analytical model for spherical galaxies and bulges. *Astrophysical Journal*, 356:359–364, 1990. doi: 10.1086/168845.

L. Hernquist. N-body realizations of compound galaxies. *The Astrophysical Journal, Supplement*, 86:389–400, June 1993. doi: 10.1086/191784.

P. Hut and J. Makino. The art of computational science: Moving stars around. October 2006. URL http://www.artcompsci.org/msa/web/vol_1/v1_web.pdf.

R. A. Ibata, G. F. Lewis, A. R. Conn, M. J. Irwin, A. W. McConnachie, S. C. Chapman, M. L. Collins, M. Fardal, A. M. N. Ferguson, N. G. Ibata, A. D. Mackey, N. F. Martin, J. Navarro, R. M. Rich, D. Valls-Gabaud, and L. M. Widrow. A vast, thin plane of corotating dwarf galaxies orbiting the Andromeda galaxy. *Nature*, 493:62–65, January 2013. doi: 10.1038/nature11717.

S. Kazantzidis. N-body realizations of cuspy dark matter haloes. master thesis, Durham University, mar 2003.

S. Kazantzidis, J. Magorrian, and B. Moore. Generating equilibrium dark matter halos: Inadequacies of the local maxwellian approximation. *The Astrophysical Journal*, 601(1):37, 2004.

A. Klypin, A. V. Kravtsov, O. Valenzuela, and F. Prada. Where Are the Missing Galactic Satellites? *The Astrophysical Journal*, 522:82–92, September 1999. doi: 10.1086/307643.

S. E. Koposov, V. Belokurov, G. Torrealba, and N. Wyn Evans. Beasts of the Southern Wild: Discovery of nine Ultra Faint satellites in the vicinity of the Magellanic Clouds. *ArXiv e-prints*, March 2015.

M. G. Lee, W. L. Freedman, and B. F. Madore. The Tip of the Red Giant Branch as a Distance Indicator for Resolved Galaxies. *The Astrophysical Journal*, 417:553, November 1993. doi: 10.1086/173334.

N. I. Libeskind, C. S. Frenk, S. Cole, J. C. Helly, A. Jenkins, J. F. Navarro, and C. Power. The distribution of satellite galaxies: the great pancake. *Monthly Notices of the Royal Astronomical Society*, 363:146–152, October 2005. doi: 10.1111/j.1365-2966.2005.09425.x.

N. I. Libeskind, A. Di Cintio, A. Knebe, G. Yepes, S. Gottlöber, M. Steinmetz, Y. Hoffman, and L. A. Martinez-Vaquero. Cold versus Warm Dark Matter Simulations of a Galaxy Group. *Publications of the Astronomical Society of Australia*, 30:e039, July 2013. doi: 10.1017/pasa.2013.16.

A. W. McConnachie. The Observed Properties of Dwarf Galaxies in and around the Local Group. *The Astronomical Journal*, 144:4, July 2012. doi: 10.1088/0004-6256/144/1/4.

A. W. McConnachie, M. J. Irwin, R. A. Ibata, J. Dubinski, L. M. Widrow, N. F. Martin, P. Côté, A. L. Dotter, J. F. Navarro, A. M. N. Ferguson, T. H. Puzia, G. F. Lewis, A. Babul, P. Barmby, O. Bienaymé, S. C. Chapman, R. Cockcroft, M. L. M. Collins, M. A. Fardal, W. E. Harris, A. Huxor, A. D. Mackey, J. Peñarrubia, R. M. Rich, H. B. Richer, A. Siebert, N. Tanvir, D. Valls-Gabaud, and K. A. Venn. The remnants of galaxy formation from a panoramic survey of the region around M31. *Nature*, 461:66–69, September 2009. doi: 10.1038/nature08327.

M. Metz, P. Kroupa, C. Theis, G. Hensler, and H. Jerjen. Did the Milky Way Dwarf Satellites Enter The Halo as a Group? *The Astrophysical Journal*, 697:269–274, May 2009. doi: 10.1088/0004-637X/697/1/269.

B. Moore, S. Ghigna, F. Governato, J. Lake, T. Quinn, J. Stadel, and P. Tozzi. Dark matter substructure within galactic halos. *The Astrophysical Journal Letters*, 524(1):L19, 1999. URL http://stacks.iop.org/1538-4357/524/i=1/a=L19.

K. Nitadori and J. Makino. Sixth- and eighth-order hermite integrator for n-body simulations. *New Astronomy*, 13(7):498 – 507, 2008. ISSN 1384-1076. doi: http://dx.doi.org/10.1016/j.newast.2008.01.010.

M. S. Pawlowski, P. Kroupa, and H. Jerjen. Dwarf galaxy planes: the discovery of symmetric structures in the Local Group. *Monthly Notices of the Royal Astronomical Society*, 435:1928–1957, November 2013. doi: 10.1093/mnras/stt1384.

Planck Collaboration, P. A. R. Ade, N. Aghanim, C. Armitage-Caplan, M. Arnaud, M. Ashdown, F. Atrio-Barandela, J. Aumont, C. Baccigalupi, A. J. Banday, and et al. Planck 2013 results. XXIII. Isotropy and statistics of the CMB. *Astronomy & Astrophysics*, 571:A23, November 2014. doi: 10.1051/0004-6361/201321534.

W. H. Press. *Numerical Recipes in Fortran 90: The Art of Parallel Scientific Computing*. Number v. 2 in FORTRAN Numerical Recipes: The Art of Parallel Scientific Computing. Cambridge University Press, 1996. ISBN 9780521574396.

T. Quinn, N. Katz, J. Stadel, and G. Lake. Time stepping N-body simulations. *ArXiv Astrophysics e-prints*, October 1997.

S. A. Rodionov and N. Ya. Sotnikova. Optimal choice of the softening length and time-step in N-body simulations. *Astronomy Reports*, 49:470–476, 2005. doi: 10.1134/1.1941489.

L. Rodriguez, J. St. Germaine-Fuller, and S. Wickramasekara. Newton-Cartan Gravity in Noninertial Reference Frames. *ArXiv e-prints*, December 2014.

J. A. Sellwood. The art of n-body building. *Annual Review of Astronomy and Astrophysics*, 25(1):151–186, 1987. doi: 10.1146/annurev.aa.25.090187.001055.

A. Sevrin. Een eerste inleiding tot de mechanica. Syllabus, VUB, September 2012. URL http://we.vub.ac.be/tena2/sites/default/files/BA1.pdf.

D. N. Spergel, R. Bean, O. Doré, M. R. Nolta, C. L. Bennett, J. Dunkley, G. Hinshaw, N. Jarosik, E. Komatsu, L. Page, H. V. Peiris, L. Verde, M. Halpern, R. S. Hill, A. Kogut, M. Limon, S. S. Meyer, N. Odegard, G. S. Tucker, J. L. Weiland, E. Wollack, and E. L. Wright. Three-year wilkinson microwave anisotropy probe (wmap) observations: Implications for cosmology. *The Astrophysical Journal Supplement Series*, 170(2):377, 2007. URL http://stacks.iop.org/0067-0049/170/i=2/a=377.

V. Springel. The Cosmological simulation code GADGET-2. *Monthly Notices of the Royal Astronomical Society*, 364:1105–1134, 2005. doi: 10.1111/j.1365-2966.2005.09655.x.

V. Springel. High performance computing and numerical modelling. December 2014. URL http://adsabs.harvard.edu/abs/2014arXiv1412.5187S.

V. Springel, J. Wang, M. Vogelsberger, A. Ludlow, A. Jenkins, A. Helmi, J. F. Navarro, C. S. Frenk, and S. D. M. White. The Aquarius Project: the subhaloes of galactic haloes. *Monthly Notices of the Royal Astronomical Society*, 391:1685–1711, December 2008. doi: 10.1111/j.1365-2966.2008.14066.x.

P. C. van der Kruit. The three-dimensional distribution of light and mass in disks of spiral galaxies. *Astronomy & Astrophysics*, 192:117–127, March 1988.

M. G. Walker, M. Mateo, E. W. Olszewski, O. Y. Gnedin, X. Wang, B. Sen, and M. Woodroofe. Velocity Dispersion Profiles of Seven Dwarf Spheroidal Galaxies. *The Astrophysical Journal, Letters*, 667:L53–L56, September 2007. doi: 10.1086/521998.

H.-H. Wang, R. S. Klessen, C. P. Dullemond, F. C. van den Bosch, and B. Fuchs. Equilibrium initialization and stability of three-dimensional gas discs. *Monthly Notices of the Royal Astronomical Society*, 407:705–720, September 2010. doi: 10.1111/j.1365-2966.2010.16942.x.

L. M. Widrow and J. Dubinski. Equilibrium Disk-Bulge-Halo Models for the Milky Way and Andromeda Galaxies. *The Astrophysical Journal*, 631:838–855, October 2005. doi: 10.1086/432710.

K. Yoshikawa and T. Fukushige. PPPM and TreePM Methods on GRAPE Systems for Cosmological N-Body Simulations. *Publications of the Astronomical Society of Japan*, 57:849–860, December 2005. doi: 10.1093/pasj/57.6.849.

P. Young. The leapfrog method and other "symplectic" algorithms for integrating newton's laws of motion. April 2014. URL http://young.physics.ucsc.edu/115/leapfrog.pdf.

H. Zhan. Optimal Softening for N-Body Halo Simulations. *The Astrophysical Journal*, 639:617–620, March 2006. doi: 10.1086/499763.